ToF-SIMS in Material Research: A View from Nanoscale Hydrogen Detection

Binod Paudel[1#], Jeffrey A. Dhas[1,2#], Yadong Zhou[3], Min-Ju Choi[1], David J. Senor[4], Chih-Hung Chang[2], Yingge Du[1], Zihua Zhu[3*]*

[1]Physical and Computational Sciences Directorate, Pacific Northwest National Laboratory, Richland, USA 99354

[2]School of Chemical, Biological and Environmental Engineering, Oregon State University, Corvallis, OR 97331, USA

[3]Environmental Molecular Sciences Laboratory, Pacific Northwest National Laboratory, Richland, USA 99354

[4]Energy and Environment Directorate, Pacific Northwest National Laboratory, Richland, Washington 99352, United States

[#] Equal contribution

[*]zihua.zhu@pnnl.gov, yingge.du@pnnl.gov

Abstract:

Hydrogen in materials has attracted tremendous interest as its incorporation leads to significant alterations in nanoscale structure, composition, and chemistry, impacting functional properties. It has also been integral to nuclear fusion reactors and is considered a future clean energy source. However, nanoscale characterization and manipulation of hydrogen in materials are challenging as only a selected few analytical techniques can readily detect hydrogen, among which time-of-flight secondary ion mass spectrometry (ToF-SIMS) is a unique and powerful one due to its excellent detection limit along with decent depth and lateral resolutions. In this review, we discuss, using selected examples, how to detect and quantify hydrogen in materials by ToF-SIMS and its impact on revealing the hydrogenation/protonation-induced novel functional states in different classes of materials. In addition, we present our protocols on sample preparation and experimental conditions optimization, allowing us to achieve the best possible results. Finally, we highlight future research directions that can lead to the discovery of novel functional states and ultimately provide a deeper understanding of scientific questions in materials science.

Keywords:

ToF-SIMS, nanoscale hydrogen detection, depth profiling, imaging, metal oxide thin film, deuterium, tritium

1. Introduction:

1.1 Why is hydrogen detection significant?

Hydrogen (H) is the simplest and most abundant chemical element in the universe, and it exists in three naturally occurring isotopes: the most common being protium ($^{1}_{1}$H, 99.98%), followed by deuterium ($^{2}_{1}$H, or D, 0.02%), and the radioactive tritium ($^{3}_{1}$H or T, present in trace amounts)[1]. Hydrogen is considered the fuel of the future as it is clean, eco-friendly, abundant, and non-toxic[2–4]. To accommodate the continual advancement towards technological development, the reliance on hydrogen will dramatically increase due to its environmental friendliness compared to conventional fuel sources and to achieve the global mission of net zero carbon in coming years[5]. Hydrogen's low mass and rapid diffusive behavior make it readily adsorb onto and desorb off materials, and its smaller activation energy leads to facile incorporation, resulting in substantial structural and functional modulations[6]. However, major concerns about its storage, handling, and bulk and sub-/surface detection prevent its efficient and secure utilization and controlled incorporation at the nanoscale.

Additionally, hydrogen is constantly drawing attention among the scientific community in material science research because it is ubiquitous and elusive in almost all materials and alters the global mass/charge distribution in those materials[7]. The degree of diffused and incorporated hydrogen

in the bulk, thin films, soft, organic, and novel quantum materials can give rise to entirely new ground states and more often, can serve as a control parameter to tune the functional properties. Since the doping and transfer of hydrogen ions is extremely facile compared to most other ions, exploration of new states in materials can be achieved by hydrogenation, which can accelerate the discovery of new materials with unprecedented properties, thereby stabilizing intermediate hydrogenated or metastable phases. Being the lightest element with the smallest size and high mobility, it is easiest to incorporate monatomic hydrogen within defect sites, interfaces, surfaces, and interstitials of bulk materials, and single- and poly-crystalline thin films to engineer the structure, chemistry, and defects [8]. Hydrogen is also inevitable in fabrication processes such as etching, surface cleaning, and doping of semiconductor thin film devices[9,10], all impacting the quality and enhancing the device functionalities. On the other hand, some materials like metals, their compounds, and alloys suffer an unwanted presence of hydrogen that can trigger embrittlement and suppress existing properties [11,12]. Since the isotopes of hydrogen (H, D, and T), have similar diffusion mechanisms and behave like H in all aspects except mass [13], H isotope labeling, or exchange[14], is commonly adopted for accurate quantification of H[15] and better understanding of its dynamics in materials. The controlled incorporation of H and its isotopes in materials warrants state-of-the-art surface and bulk H detection techniques that can readily capture the process of hydrogenation and guide for the design of concomitant phases with desired properties. First-hand H detection capability of ToF-SIMS is thus crucial to gain insights on H-induced properties of materials across various areas of applications, as summarized in **Figure 1**.

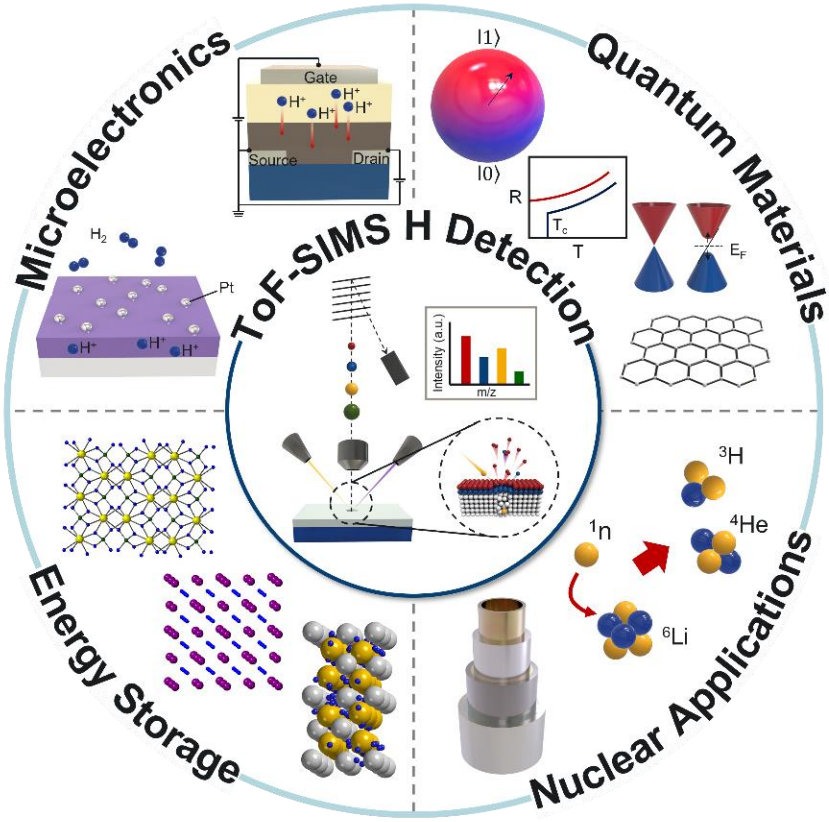

Figure 1: H detection in materials via ToF-SIMS for applications in some critical scientific directions.

Microelectronics and Optoelectronics. H is paramount in the thin films of strongly correlated oxide and semiconducting materials because its fast incorporation drives facile modulations in lattice, electronic, and magnetic degrees of freedom [7,16–23]. For instance, electrochemical incorporation or removal of H at the nanoscale has induced electronic phase transformations and opened possibilities for novel conducting devices in strongly correlated oxide thin films [24–28]. Hydrogenation has induced reversible insulator-to-metal transitions in prototype VO_2 and WO_3

thin films, thus offering an extra dimension to tailor the properties in strongly correlated oxides[27,29,30]. Since the structural phase transitions accompany the reversible metal-insulator transitions, hydrogenation can also distort lattices by expanding the volume of unit cells in metal oxides[31,32]. Moreover, H in ZnO thin films has enhanced the conductivity by increasing n-type carriers, and intentional H has been incorporated to passivate the dangling bonds in semiconductors thin films (i.e., Si, SiO_2) to tune their electronic states[7,16,33]. The process of hydrogenation in thin films is often controlled at the nanoscale; thus, its detection in nanometer ranges is essential for the successful design of novel microelectronics architectures.

Nuclear Applications. T, the radioactive isotope of H, has a half-life of 12.3 years. Thus, it must be continuously replenished to maintain its steady supply for the strategic stockpile and power generation from nuclear fusion reactions[34]. The ^{6}Li-rich γ-$LiAlO_2$ pellets are used in tritium-producing burnable absorber rods (TPBARs) to breed T through thermal neutron irradiation because of their excellent behavior against irradiation at high temperatures and show more swelling resistance than many other Li-rich compounds[35,36]. A comprehensive understanding of the diffusion pathways of H species is needed at temperatures where T is produced [37]. Thus, irradiation-induced profiles investigation in TPBARs as a function of irradiation doses and temperatures warrants an excellent H detection technique. In addition, nuclear wastes can be immobilized into a glass matrix for long-term storage[38,39]. Water corrosion of such nuclear waste glass is of great interest because such corrosion may lead to the release of radioactive wastes into the environment[40,41]. H detection provides important information to evaluate the glass corrosion process [42,43] quantitatively.

Quantum Materials. H is a common reducing agent extensively utilized in the form of CaH_2 for the soft topotactic reduction of various transition metal oxides[44,45], which results in infinite layered structures offering quantum phenomena such as superconductivity[46,47]. However, this leads to an unwanted H incorporation in metal oxide lattices, and can severely suppress electronic properties and alter the band structures[48,49]. Moreover, niobium-based superconducting qubits have shown significant drop in coherence times due to the inward diffusion of niobium hydrides as impurity species as a result of H incorporation during the fabrication of qubits[50]. Facile doping of H in topological insulators has effectively modulated the carrier density and tuned the Fermi level without changing carrier mobilities[51]. These selected studies highlight why nanoscale H detection is significant in improving the functionalities of quantum materials that can be harnessed for accessible device platforms.

Hydrogen Storage. Material-based H storage is another area worth mentioning for the application of H detection. For example, rare earth metals readily absorb and desorb H and its isotopes at ambient temperature in the transition, forming fluorite-type structured metal hydrides. Since these structures do not dissociate easily, erbium hydrides (ErH_2, ErD_2, or ErT_2) often serve as model systems and can be apparent candidates to investigate the solid state H storage capabilities[52–54]. Moreover, complex metal hydrides[55] and metal-organic frameworks[56], undergo reversible intake of T and D, mostly stored within the interstitial sites, thereby motivating the robust nanoscale detection of H and its isotopes.

1.2 Challenges for nanoscale hydrogen detection:

Despite reversible H incorporation in metal oxide lattices being fast, facile, and recognized as a knob to regulate the properties of materials, its detection, and manipulation at the nanoscale is quite challenging. Traditionally, inert gas fusion (IGF) and thermal desorption spectroscopy (TDS)

were widely employed to quantitatively detect H concentration in various materials [57–59]. However, these methods are bulk analysis techniques that can only measure total H within the system, making them ineffective if the detection of nanoscale or local distribution of H is desired. Additionally, most of the popularly used material characterization techniques that work based on electron and X-ray interactions, such as transmission electron microscopy (TEM), scanning electron microscopy (SEM), X-ray photoelectron spectroscopy (XPS), and X-ray diffraction (XRD), can provide indirect H signatures, but their weaker interactions with H due to low electron density in H prevents the direct direction of H.

Only a few techniques can enable nanoscale H detection. The following table compares detection limits, quantification ability, depth resolution, lateral resolution, instrument availability, sample preparation, and analysis time cost among these techniques. A color-coded ranking system is implemented to compare each, highlighting strengths, weaknesses, and how they can complement one another for H detection applications.

Table 1. Table of Complementary Techniques in Nanoscale Detection of Hydrogen

Technique	**ERDA**	**NRA**	**APT**	**Magnetic SIMS**	**NanoSIMS**	**ToF-SIMS**
Detection Limit	< 1 at %	< 0.1 at %	< 1 at %	< 0.01 at %	< 0.01 at %	< 0.01 at %
Quantification Ability	Quantitative	Quantitative	Semi-Quantitative	Semi-Quantitative	Semi-Quantitative	Semi-Quantitative
Depth Resolution	~ 50 nm	< 50 nm	< 0.5 nm	< 1 nm	< 10 nm	< 1 nm
Lateral Resolution	Rarely reported	Rarely reported	< 0.5 nm	~ 0.5-1.0 μm, less used	~ 50 nm	~ 100 nm
Instrument Availability	Low	Low	Medium	Medium	Low	High
Sample Preparation	Easy	Easy	Complex	Some tricks	Some tricks	Easy
*Relative Time for Testing & Data Analysis**	1	1	> 4	1	>2	1

Good	Better	Excellent

* Example: NanoSIMS takes approximately 2x longer than ToF-SIMS for sample testing and data analysis.

Nuclear-based techniques such as elastic recoil detection analysis (ERDA) and nuclear reaction analysis (NRA) have been used to detect H within bulk materials [60–65]. In ERDA, the yield of recoiled H is proportional to the concentration of H within the material. Using the intensity of the incident beam and accounting for the geometry of the experimental setup, ERDA can achieve quantification ability with a roughly 1% (atomic ratio) detection limit [59,66]. NRA utilizes a beam of accelerated and energy-monochromatized ions that induce nuclear reactions with H within the sample, thereby producing α and γ rays, which are used for the detection and quantification of H. Detection limit of about 0.1% (atomic ratio) is achievable using NRA, which when coupled with a depth resolution of < 50 nm makes it a comparatively better method than ERDA for H depth profiling applications [59]. Unfortunately, the micron-scale lateral resolution of ERDA and NRA makes nanoscale H imaging difficult[67–69]. Additionally, highly complex instrumentation (i.e., particle accelerators, high-energy ion beam optics, and required detection systems) and limited availability make ERDA or NRA an unfavorable first choice for H depth profiling and imaging but exceptional complimentary techniques for H quantification [59].

Atom probe tomography (APT) is another technique used for H (or related isotopes) detection, commonly in metals, alloys, and oxide samples [70–74]. Layer-by-layer evaporation of the sample of interest yields ultimate depth and spatial resolution among the techniques discussed [75]. A key limitation for H detection in APT is the high H background, which adversely affects the detection limit of the technique. H can be artificially introduced into the material during Ga-focused ion beam (FIB) milling for sample preparation. Also, residual gases (such as H_2O, H_2, hydrocarbon) in the stainless-steel chamber can adsorb onto the APT sample tip, causing high background signal during field evaporation [76,77]. The use of titanium parts [77] and cryogenic Xe plasma FIB

(cryo-PFIB) can mitigate the introduction of artefactual H by minimizing the thermal-assisted diffusion processes of H onto the sample tip [78]. Ultimately, tedious sample preparation, high H background signal, lengthy analysis time, and relatively small field-of-view make APT a high-cost and low throughput choice compared to ToF-SIMS. However, superior spatial resolution makes APT an excellent complementary technique for site-specific H imaging and depth profiling applications.

Within the SIMS technique, different mass analyzer types can complement each other to provide holistic information for H detection. While ToF-SIMS is the most convenient technique given its high instrument availability, regular magnetic SIMS and NanoSIMS are two additional methods that can be complementary. For depth profiling applications, the depth resolution of ToF-SIMS can be comparable to regular magnetic SIMS, and both are better than NanoSIMS. Detection limits of D and T using regular magnetic SIMS usually is 1-2 orders of magnitude better than ToF-SIMS, but they show similar detection limits in H detection because the major limitation in H detection is background H signals from residual gases [79,80]. The NanoSIMS shows better lateral resolution, which is useful for H imaging in materials while maintaining similar preparation procedures [81–84]. Furthermore, ToF-SIMS has the advantage of a full mass spectrum range, making it very useful in simultaneous multi-component detection and failure analysis. Overall, the complementarity of each proves the SIMS family to be a powerful depth profiling and imaging technique for H detection studies.

1.3 Time-of-flight secondary ion mass spectrometry (ToF-SIMS):

SIMS is a powerful tool that can examine the nanoscale distribution of H in various materials[79,80,85–88]. In SIMS, a focused primary ion beam is used to sputter sample surfaces to eject secondary ions that can be analyzed by either of the analyzers: time-of-flight, magnetic

sector, or quadrupole. A time-of-flight mass analyzer is capable of examining mass-to-charge ratios (m/z) of secondary ions of all elements in the periodic table, including H simultaneously (**Figure 2b**). Among all SIMS techniques, ToF-SIMS is the most versatile one as it can provide elemental, molecular, and isotopic analysis of surfaces with reasonably high mass, depth, and lateral resolutions (Table 1). Since many of the scientifically significant properties of the materials are governed by the chemical structures of the uppermost layers of atoms/molecules on the surface, the surface sensitivity of ToF-SIMS finds applications in the semiconductor industry, advanced materials science, complex biological research, and more [89].

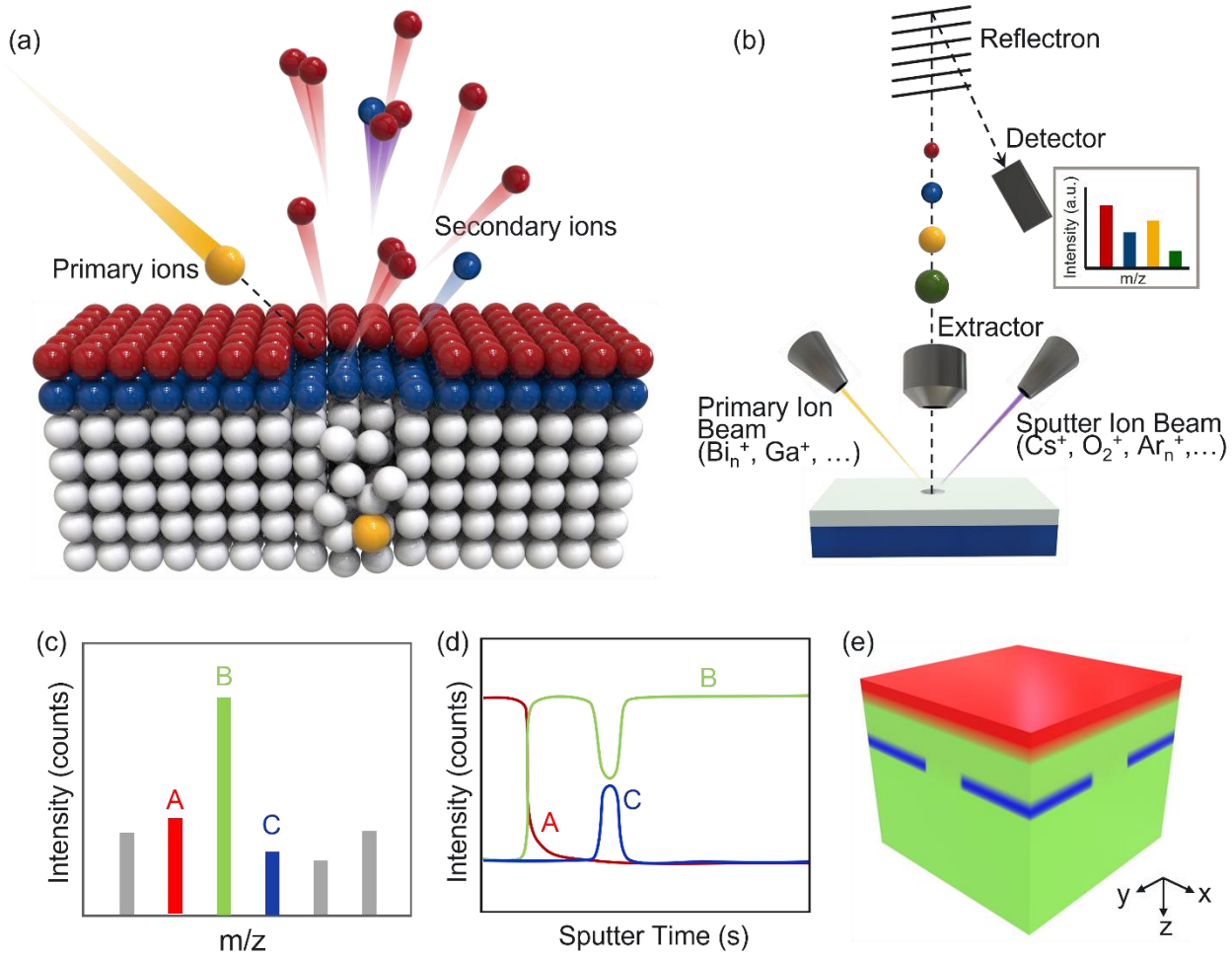

Figure 2: A schematic illustration of the ToF-SIMS principle and typical data sets of ToF-SIMS analysis. (a) Primary ions impact the solid sample surface to eject secondary ions. Secondary ions from only the top 1-2 atomic layer species can escape as SIMS is surface sensitive. (b) Time-of-flight principle. An electric field is added between the extractor and substrate to accelerate secondary ions for mass analysis; normally, only one polarity, either positive or negative ions, can be analyzed in a measurement. Most secondary ions have only one charge, and all ions get the same energy in an electric field for flight. A lighter ion acquiring faster speed will reach the detector early and a heaver ion with smaller energy reaches later. Based on time-of-flight, m/z values of secondary ions can be determined. (c) a mass spectrum, (d) depth profiles, and (e) 3D ion maps of interesting ion species in (c).

ToF-SIMS can be used for static SIMS analysis where the sample surface (1-2 atomic layers) can be regarded as intact due to a low dose of the primary ions ($< 1\times10^{12}$ ions/cm^2) with little sputtering (< 0.1% of a monolayer) during the data acquisition[89–93]. This technique is very useful for qualitative surface analysis as it offers high mass resolution (5000+) spectra (**Figure 2c**) for molecular identification of surface species, high sensitivity for trace species analysis (ppm to ppb for most species), as well as submicron lateral resolution (50-100 nm) imaging for elucidation of the spatial distribution of interesting species. In addition to the static surface analysis, it is also capable of dynamic analysis with the depth-resolved chemical profile, i.e., depth profiling (**Figure 2d**). For this purpose, along with an analysis primary ion beam, a sputtering ion beam can be used to erode the materials from the surface at a reasonable rate for subsequent layer-by-layer analysis. Such layer-resolved analysis mode is called “dual-beam analysis”[92–94]. The selection of the sputtering beam depends upon several factors including the type of chemical species of interest,

variation of the ion yields, matrix effects, etc. [89,95,96]. A combination of 2D imaging and depth profiling can yield high-resolution 3D images that are shown in **Figure 2e**.

2. H-detection by ToF-SIMS in material research: Applications

2.1 Depth profiling or depth-resolved detection:

Two widely used approaches that lead to controlled hydrogenation or protonation of materials are electrochemical hydrogen insertion[26,27,97–101] and catalytic hydrogen spillover[24,31,102–106]. Recently, metal-acid treatments of thin films have also demonstrated hydrogenation as the acid solution provides a rich natural proton source and is capable of bulk doping[51,107–109]. Electrochemical incorporation refers to H incorporation by applying electric fields with solid/liquid and solid/solid interfaces that inject H in the form of a proton and an electron, leading to a nearly uniform H concentration from surfaces to the film interfaces, **Figure 3b**. However, the resulting properties' modulations are mostly interpreted as of electronic origin manifested by the changes in metal valence states, which, in turn, modifies the band gaps[24,98,110], electron antidoping mechanisms [111], while the status of protons and their effects are often poorly understood [24,110,112,113]. On the other hand, the hydrogen spillover route enables the doping of materials via the diffusion of monatomic H, which predominantly resides at the interstitial sites [7,31,102,114] and incorporates a gradient of H within the films, **Figure 3c**. Moreover, the surface-adsorbed and bulk-absorbed H interact differently with the materials resulting in distinct physio-chemical properties. Thus, the quantification of site-dependent H incorporation enables a new approach to engineer materials for desired properties, which attracts enormous interest in material science to utilize techniques that allow for depth-resolved H detection from surfaces to buried interfaces.

Various strongly correlated complex oxides have been studied in recent years as model systems for hydrogenation-mediated property switching. For instance, the metal-insulator transitions in archetypical strongly correlated oxide VO_2 are being modulated by electrochemical as well as hydrogen spillover routes [25,27,31,114]. The varied H concentrations due to the tuning of an applied electric field voltage results in hydrogenated metastable phases with entirely unique lattices thereby leading to exotic electronic states[27,31,101]. To explore the field induced non-volatile switching devices, it is important to understand the field-induced chemical profiles and H^+ and other ions doping/incorporation along the z-direction and its subsequent property changes.

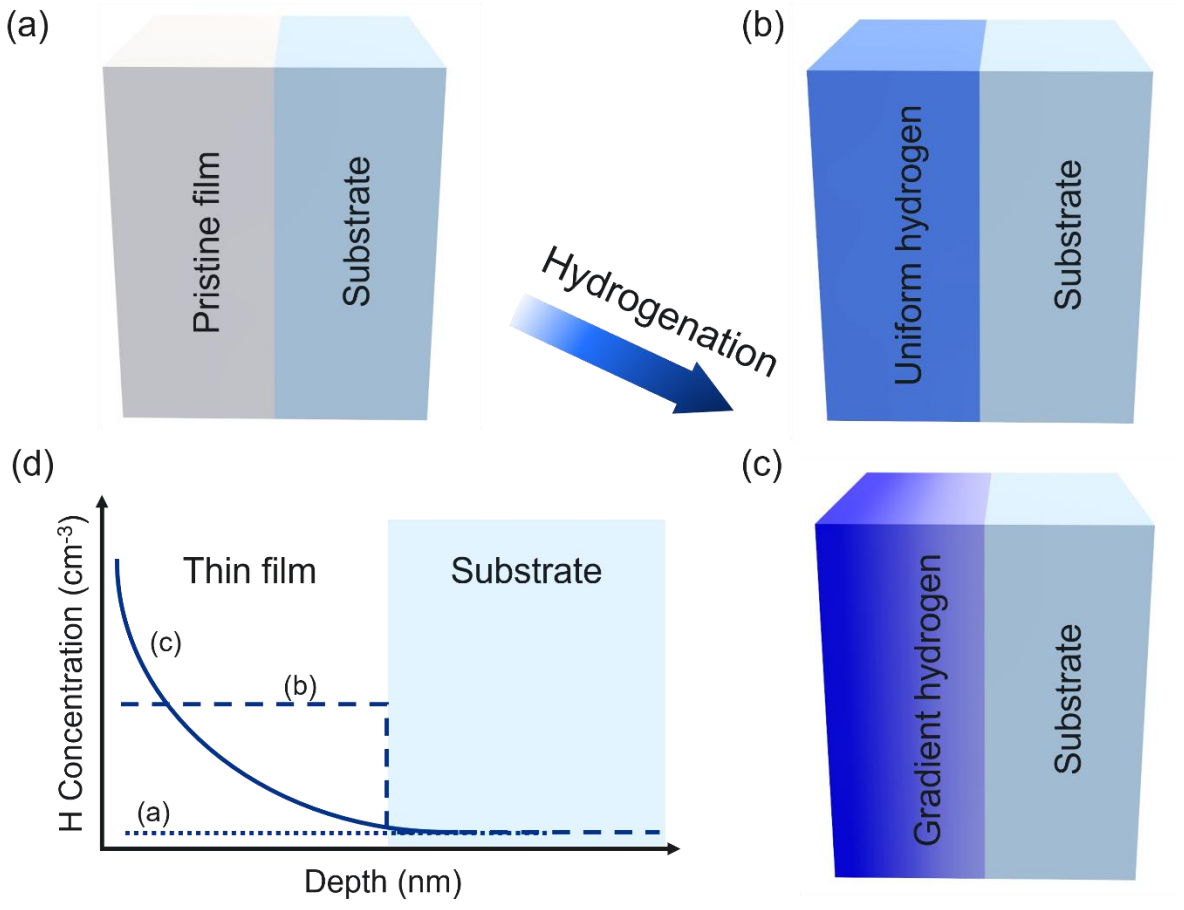

Figure 3: Nanoscale hydrogenation and ideal SIMS depth profiles in thin films. (a) Pristine thin film before hydrogenation. (b) Film after hydrogenation with a uniform H profile, mostly observed

via electrochemical incorporation. (c) Non-uniform H-profile with a gradient from surface to the interface observed via hydrogen spillover, and (d) corresponding H depth profiles for the pristine and hydrogenated thin films via two different routes. Substrate H-depth profile is used to demark the films and substrate interface.

It is well known that the electrolyte or ionic liquid gating in field effect transistor (FET) devices can modulate the charge carriers at the electrolyte and the channel material interface, causing an excess in charge carrier density (10^{14} cm^{-2}) [25]. To understand what triggers such excess density and how the enhanced carriers alter the electronic states in thin films, liquid ion gating in VO_2 thin film devices was performed. This prototype device, an electric double-layer transistor (EDLT), undergoes a reversible insulating to metallic transition when gate voltages are increased from 0 to 0.8 V and vice versa, as shown in **Figure 4a**. As demonstrated by the Raman spectroscopy, as shown in **Figure 4b**, the gated device subsequently undergoes substantial structural modifications compared to the pristine one.

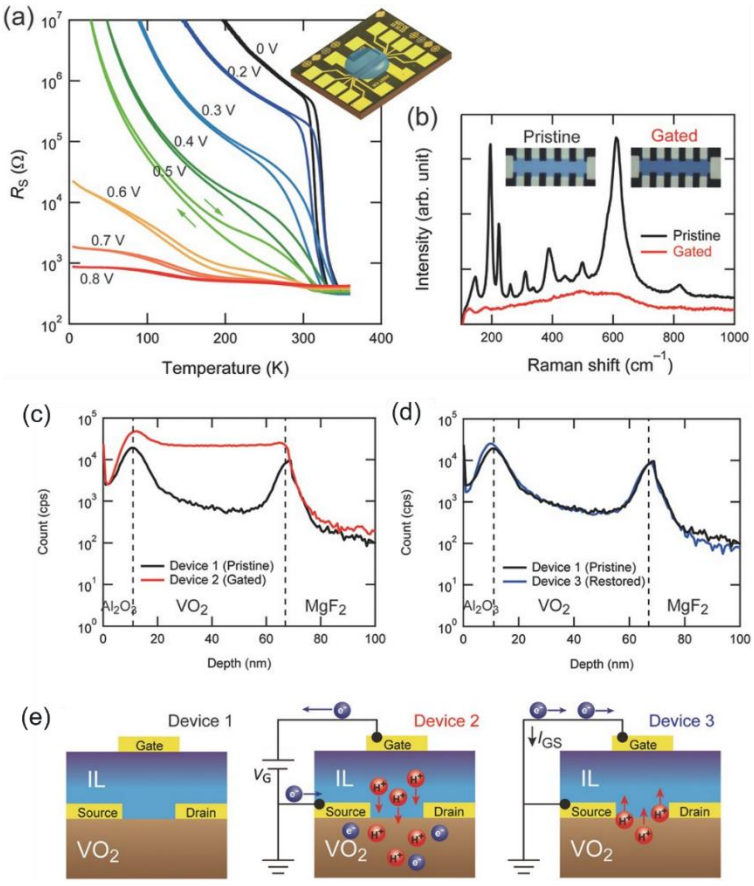

Figure 4: Electronic state modulations of VO_2 thin films with applied voltage and H depth profiles on different EDL devices. (a) Temperature vs. sheet resistances of the EDLTs based on VO_2 films at various gate voltages. The inset shows a schematic of a typical EDL device. (b) Raman scattering spectra for pristine and hydrogenated VO_2 film via ion gating. (c, d) H-depth profiles of pristine and gated devices of VO_2. (e) Schematics of EDL devices 1, 2, and 3 in pristine, gate-induced protonated (Device 2), and restored to the pristine states, respectively [25].

To reveal the drivers of field-induced electronic states switching, ToF-SIMS H depth profiling was carried out in three devices as depicted in **Figure 4c, d**. Interestingly, the same device with and without gate voltage shows pronounced variations in H concentration. In particular, the device 2 experiences a nearly two-fold increase in H concentration compared to device 1 while applying V_G = 1.2 V. The H concentration is observed to be decreased to the level of device 1 when the

gated device was restored to the pristine state, i.e., device 3, **Figure 4d, e**. These findings revealed by the SIMS depth profiling suggest that the gate voltage drives the H incorporation into the VO_2 channel, switching the device into the metallic state. Conversely, the removal of the gate voltage leads to the decrease in H concentration from device 2, reverting it to its original insulating state. This example of direct H detection highlights the importance of understanding H incorporation's role in realizing the functional devices that show potential for oxide electronics.

Similar scientific questions were also addressed in thin films of WO_3 and $SrCoO_{2.5}$ (SCO), where an electrochemical emergence of new electronic and magnetic states was explored by liquid ion gating, as seen in **Figure 5a**. The voltage biasing creates an EDL that results into a giant charge modulation within a nanometer range at the film and electrolyte interface [26,97]. The positive biasing of 3.5 V in SCO triggers a highly resistive and weakly ferromagnetic state that was otherwise a less resistive insulating and antiferromagnetic state at room temperature in its pristine brownmillerite (BM) SCO phase, while the removal of positive biasing reverts this intermediate phase back to the original BM phase as shown in **Figure 5b, c**. On the other hand, negative biasing of SCO leads to its perovskite phase ($SrCoO_{3-\delta}$), establishing a metallic as well as ferromagnetic phase, and the BM phase of SCO with its electronic and magnetic phases can be restored through the removal of biasing. The study resorted to ToF-SIMS depth profiling to understand the biasing-driven reversible electronic and magnetic switching. It is discovered that the positive biasing has developed a H-rich $HSrCoO_{2.5}$ phase, with a nearly 1000-fold increase in uniform H incorporation throughout $HSrCoO_{2.5}$ compared to its perovskite and BM counterparts deposited on LSAT substrate, **Figure 5e**. Negative biasing, however, decreases H incorporation and starts facilitating oxygen incorporation accompanied by switching states. Even though the ion-liquid gating induced non-volatile switching of functional states can be indirectly revealed through other techniques, the

direct quantification of H content and understanding of its profiles through ToF-SIMS would be instrumental to interpreting experimental data predicting hydrogenated metastable phases for the effective manipulation of materials for improved properties.

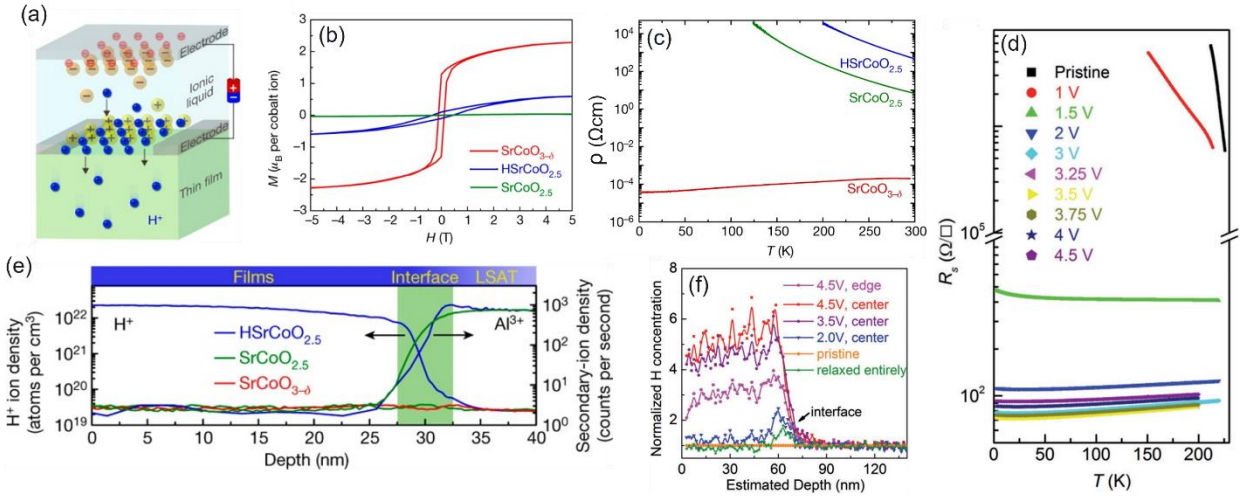

Figure 5: Ionic liquid gating driven electronic and magnetic modulations in WO_3 and $SrCoO_{2.5}$ thin films. (a) H incorporation via positive biasing of ionic liquid gating in SCO thin film. (b) Modulations of magnetic states and (c) electronic states owing to the switching of biasing voltages in liquid ion gating. (d) New electronic states due to the liquid ion gating in WO_3 thin film. (e) ToF-SIMS H depth profiles on tri-phases of the SCO films and (f) on WO_3 films with varied positive biasing [26,97].

It has been reported in the strongly correlated thin films that the flipping of voltage biasing switches the incorporation between hydrogen and oxygen ions. However, in WO_3 thin films, it is observed that both positive and negative gate voltages have varied the incorporation of only oxygen ions [29] unlike the scenarios reported in VO_2 thin films. As seen in **Figure 5d,** the gradual increase of positive bias has been switching an electronic phase of WO_3 from insulating to metallic with a sharp resistivity drop observed at 1.5 V and saturated resistivity around 3.5 V. To examine

if the positive biasing indeed involves the incorporation of hydrogen or oxygen ions, ToF-SIMS depth profiling was conducted. It is observed that the positive biasing incorporates H, which increases as a function of the gate voltages, as shown in **Figure 5f**. Upon the removal of gate voltage, the film entirely reverts to its insulating state with a complete extraction of H ions. ToF-SIMS depth profiling demonstrates that electric field-induced reversible phase emergence is primarily due to the intercalation or desorption of H ions in metal oxide thin films.

During the fabrication and processing of superconducting devices, random access memories, and quantum devices, device passivation and defect alleviation at the device interfaces are achieved through forming gas annealing with hydrogen [50,115,116]. However, the H-induced degradation in the thin film devices is a critical problem for their performance. For example, annealing of a ferroelectric capacitor Pt-(Pb,La)(Zr,Ti)O_3 (PLZT)-Pt in the forming gas (3% or 5% H_2/N_2) shows a significant reduction in remanent polarization, increase in positive coercive voltage, and a decrease in negative coercive voltage, as shown in **Figure 6d**. To understand this behavior of capacitors under annealing, ToF-SIMS depth profiling was utilized, which detects an order increase in H^- intensity in the annealed capacitor compared to the as-grown capacitor. However, no changes are observed in the concentration of chemical species such as TiO^-, ZrO^- in both cases, as shown in **Figure 6b, c**. Furthermore, ToF-SIMS depth profiling reveals an enhanced H diffusion throughout the PLZT capacitors with Pt-electrodes compared to those without, which is likely due to the catalytic behavior of the Pt-electrodes.

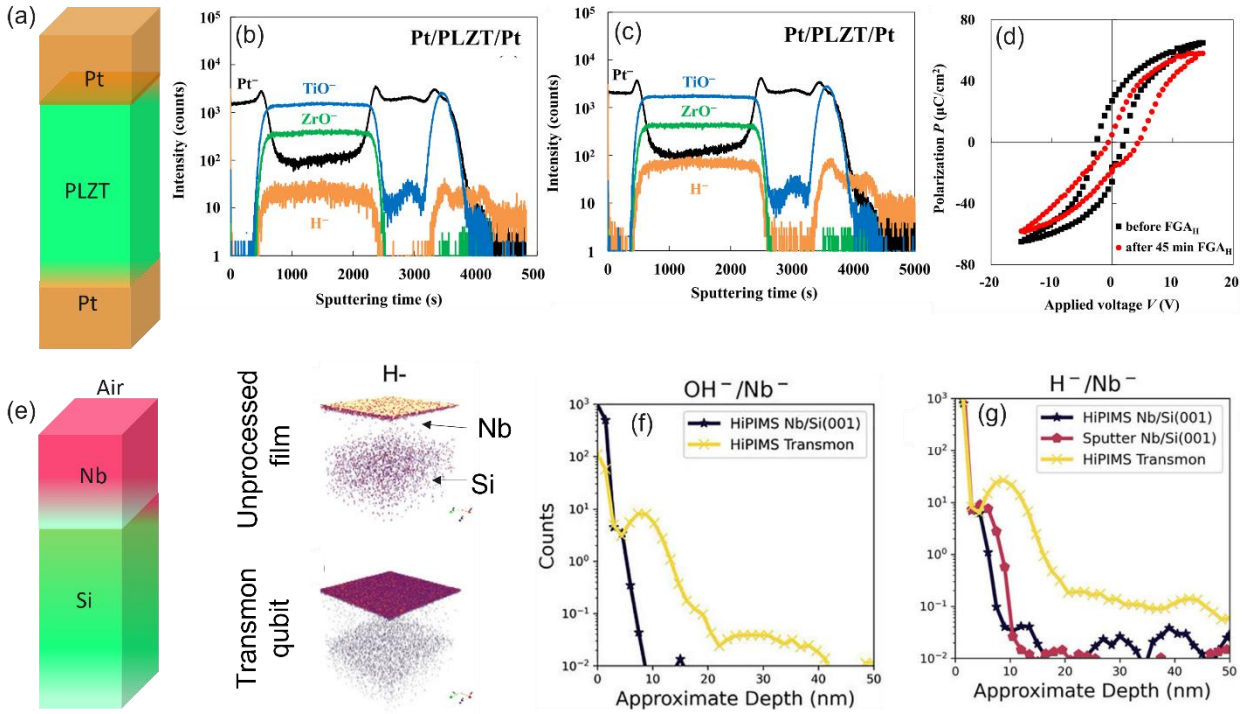

Figure 6: ToF-SIMS depth profiles of the Pt/PLZT/Pt capacitor, semiconducting Nb/Si films, and Transmon qubits for the direct detection of H. (a, e) Schematics of a capacitor and a Nb-film. (b) ToF-SIMS depth profiling of the as-grown and (c) H_2-forming gas annealed capacitor. (d) Ferroelectric properties of the capacitor [116]. (f, g) H detection in Nb/Si films and processed Transmon qubits via ToF-SIMS depth profiling[50].

The performance of the quantum devices is strongly tied to surface morphology, material quality, and interfacial abruptness. For instance, the two-level-system (TLS) defects in superconducting (SC) qubits can significantly reduce the coherence times well below the millisecond, while the longer coherence times in the range of seconds are necessary for the functioning of scalable quantum devices [50,117]. Niobium (Nb) thin films have been widely utilized for the realization of superconducting qubits, especially Transmon qubits, due to their growth compatibility with silicon CMOS architectures [118]. However, the amorphous oxide layers of Nb that usually host

TLS defects and additional chemical impurities have reportedly been responsible for the larger microwave losses, limiting the coherence times [119].

ToF-SIMS depth profiling was performed on Nb/Si(001) stack and the processed Transmon qubits to explore the suppression of coherence times in SC qubits. Interestingly, as seen in **Figure 6e,** inward diffusion of the surface H layer into the qubit compared to the as-grown film is observed. Furthermore, the H^- and OH^- depth profiles corroborate the significant H diffusion throughout the qubits fabricated after the subsequent lithography patterning of the films, shown in **Figure 6f, g**. This suggests that the H incorporation is detrimental to the qubit coherence times, and a cutting-edge ToF-SIMS depth profiling technique can inform H incorporations in the TLS defects within SC qubits and provide guidance for tailored synthesis and processing of advanced design architecture.

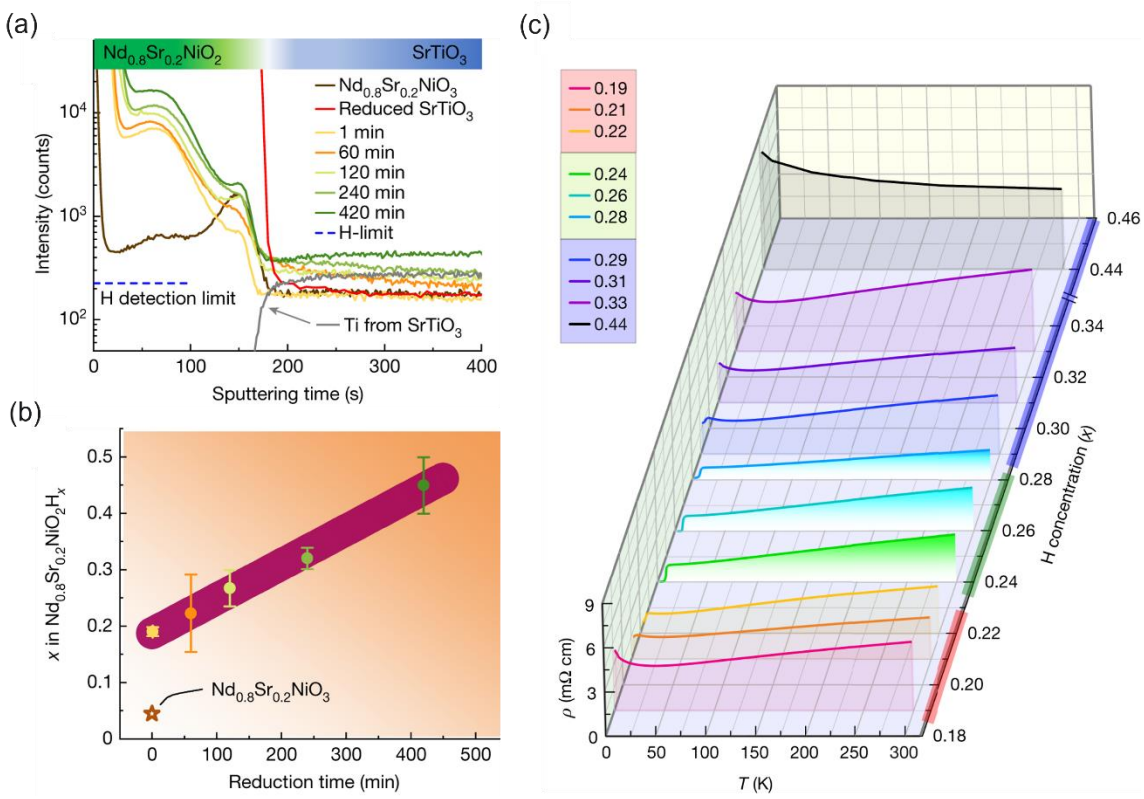

Figure 7: ToF-SIMS and transport properties measurements on $Nd_{0.8}Sr_{0.2}NiO_3H_x$ films[46]. (a) Depth profiles of pristine $Nd_{0.8}Sr_{0.2}NiO_3$ and $Nd_{0.8}Sr_{0.2}NiO_2$ films under different reduction times. (b) Quantification of H doping concentration as a function of reduction time. (c) Temperature vs. resistivity was measured for samples with different H concentrations (*x* from 0.19 to 0.44), indicating superconductivity only preserves within a narrow doping range.

Reduction of the perovskite nickelate thin films with metal hydrides (CaH_2) is an important step to realize its infinite layer superconducting phase, where the H de-intercalates the apical oxygen atoms from the NiO_6 octahedra and, in turn, reduces $RNiO_3$ into $RNiO_2$. This process usually leads to the unintentional incorporation of H that results in the formation of an H-doped phase, i.e., $RNiO_2H_x$ instead of $RNiO_2$ [46,49,120]. However, it is unclear how the superconducting properties of $RNiO_2H_x$ behave with the doping concentration of H, and most characterization techniques cannot detect H to provide insights into this critical issue.

To address this, ToF-SIMS was used to quantify the value of x in $Nd_{0.8}Sr_{0.2}NiO_3H_x$ as a function of the reduction time of $Nd_{0.8}Sr_{0.2}NiO_3$ with CaH_2, **Figure 7**. The H content on the samples during different time intervals is estimated based on the reference H-concentration detected from the mica samples. From the depth profiling of each sample, it is clearly observed that the H-concentration is linearly increased with the reduction time, **Figure 7a, b**, suggesting more H gets incorporated with the longer reduction time. The transport measurements of the samples reveal that the degree of H-incorporation is critical for superconductivity as the zero resistivity was only achieved for a narrow doping range of $0.21 \leq x \leq 0.28$, showing weakly insulating behavior for the over- and under-doped films, **Figure 7c**. These examples highlight the unique capability of ToF-SIMS, showing that its application can extend to all thin films where H doping is either desirable or unavoidable.

^{6}Li isotope enriched bulk γ-$LiAlO_2$ is an extremely critical material for T production as it has an excellent behavior compared to any other ^{6}Li-rich materials at high-temperature neutron irradiation. During irradiation, a ^{6}Li atom captures a neutron and produces a ^{4}He atom and a T atom with energies of 2.75 MeV and 2.05 MeV, respectively[37]. During irradiation, the T in $LiAlO_2$ diffuses through the material, and some of it leaves to be captured in other components within the tritium-producing burnable absorber rods [121] [122]. Thus, a fundamental understanding of diffusion and retention mechanisms of T within the γ-$LiAlO_2$ pellets is of great importance. However, due to the radioactive decay of T, H, and D are widely used as surrogates that can be introduced into the $LiAlO_2$ by ion implantation.

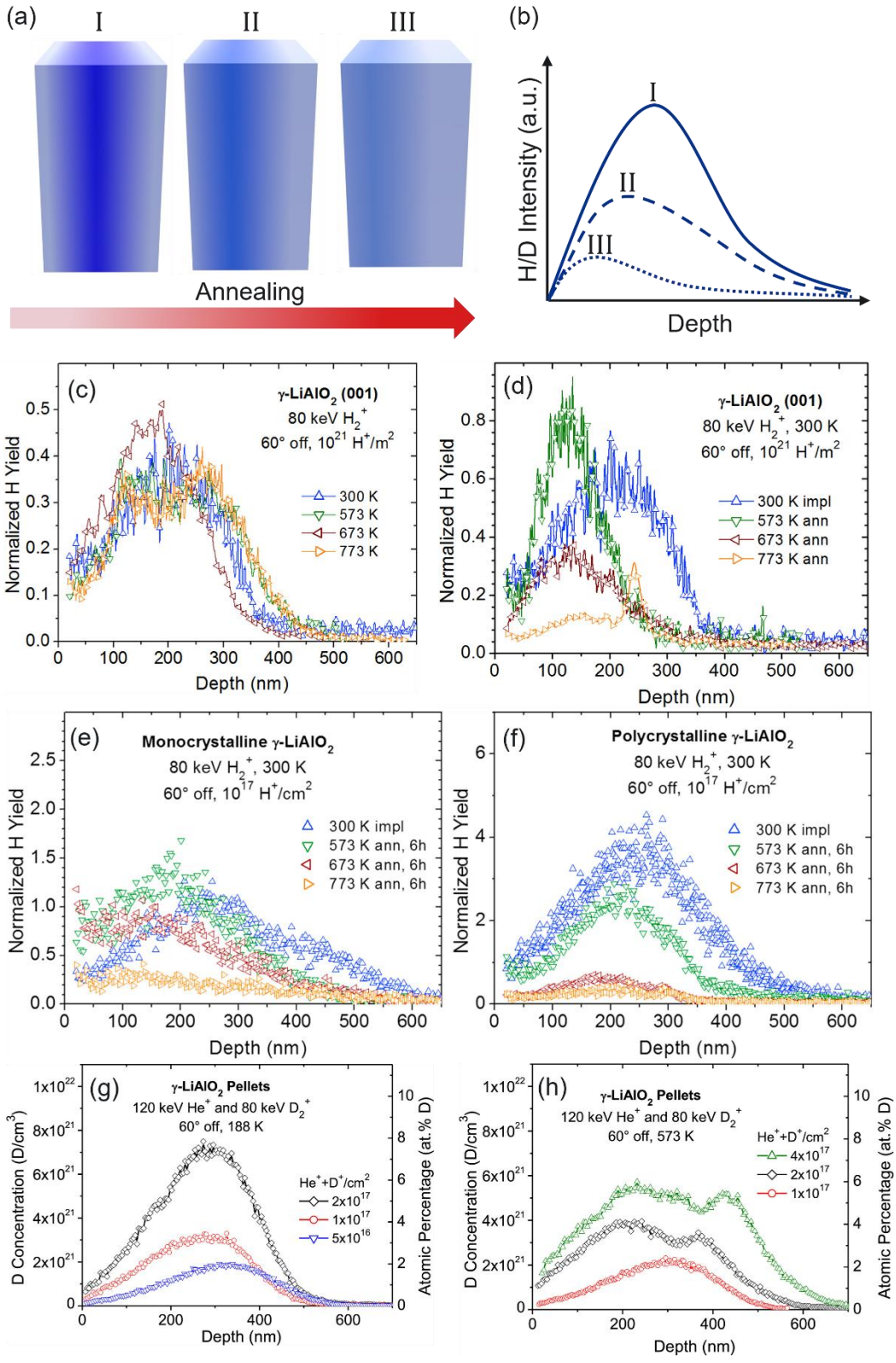
(a)
I
II
III
Annealing
(b)
H/D Intensity (a.u.)
I
II
III
Depth
(c)
γ-LiAlO2 (001)
80 keV H2+
60° off, 10^21 H+/m2
300 K
573 K
673 K
773 K
Normalized H Yield
Depth (nm)
(d)
γ-LiAlO2 (001)
80 keV H2+, 300 K
60° off, 10^21 H+/m2
300 K impl
573 K ann
673 K ann
773 K ann
Normalized H Yield
Depth (nm)
(e)
Monocrystalline γ-LiAlO2
80 keV H2+, 300 K
60° off, 10^17 H+/cm2
300 K impl
573 K ann, 6h
673 K ann, 6h
773 K ann, 6h
Normalized H Yield
Depth (nm)
(f)
Polycrystalline γ-LiAlO2
80 keV H2+, 300 K
60° off, 10^17 H+/cm2
300 K impl
573 K ann, 6h
673 K ann, 6h
773 K ann, 6h
Normalized H Yield
Depth (nm)
(g)
γ-LiAlO2 Pellets
120 keV He+ and 80 keV D2+
60° off, 188 K
He+D+/cm2
2x10^17
1x10^17
5x10^16
D Concentration (D/cm3)
Atomic Percentage (at.% D)
Depth (nm)
(h)
γ-LiAlO2 Pellets
120 keV He+ and 80 keV D2+
60° off, 573 K
He+D+/cm2
4x10^17
2x10^17
1x10^17
D Concentration (D/cm3)
Atomic Percentage (at.% D)
Depth (nm)

Figure 8: Direct ToF-SIMS detection of depth-dependent H/D diffusion/retention. (a) A schematic lustration of thermal annealing induced H/D diffusion/retention in critical materials. (b) Corresponding depth profiles for different stages of annealing. (c) H depth profiles in γ-$LiAlO_2$ (001) substrates with 80 keV H_2^+ ions implanted at different temperatures and (d) at different annealing temperatures after implanted at 300 K[37]. (e) H-depth profiles with the same H_2^+ ion doses within monocrystalline and (f) polycrystalline γ-$LiAlO_2$ pellets [121]. (g) D depth profiles in γ-$LiAlO_2$ pellets with 120 keV He^+ and 80 keV D_2^+ ions with varied doses implanted at 188 K and (h) 573 K[123].

ToF-SIMS depth profiling is key to gaining insights critical to unraveling the damages induced by T diffusion and release as a function of H_2^+ ions irradiation doses and annealing temperatures, shown in **Figure 8**. There are no significant changes in H-diffusion within γ-$LiAlO_2$ (001) single crystal substrates while implanting ions at different temperatures (300 K-773 K); however, for ion implantation at 300 K, H-diffusion is greatly affected by the thermal annealing at elevated temperatures (573 K-773 K) [37], **Figure 8c, d**. Interestingly, stronger H-retention is observed at the lower annealing temperatures (300 K-573 K) in the polycrystalline γ-$LiAlO_2$ compared to its monocrystalline counterpart for similar ion doses, while less H-retention is observed at the higher annealing temperature [121]. Such observations indicate that more grain boundaries in polycrystalline samples can host more H at low temperatures but can also serve as H diffusion channels at higher temperatures, **Figure 8e, f**. In another study, the linear increase in D retention is observed while increasing the ion fluences for a given ion energy at 188 K, **Figure 8g**. An additional irradiation of the pellets with the same ion energy indicates that the decreased D retention for 2×10^{17} $He^+ + D^+/cm^2$ fluence at 573 K is quantitatively consistent with the amount of released T from the pellets during neutron irradiation at 573 K [123], **Figure 8h**. Such studies

are critical for quantifying T retention and release in γ-$LiAlO_2$ under neutron irradiation by exchanging D in different ion irradiation conditions.

Understanding ion exchange is a topic of great interest to gain mechanistic insights into glass corrosion during the storage of high-level nuclear wastes[124–128]. It is known that H^+ can replace alkali metal ions such as Li^+, Na^+, and K^+ within the glass containment vessels, leading to subsequent degradation via corrosion[40]. ToF-SIMS plays a unique role in studying such ion exchange processes [42,43,129–136]. One study by *Stéphane et al.* showed via ToF-SIMS depth profiling that the gradients of mobile species in borosilicate glass, such as boron (B), sodium (Na), and calcium (Ca), are anticorrelated with that of H, highlighting the importance of the technique in revealing ion exchange processes for glass corrosion applications[137].

Identifying the ion-electron transfer pathways that drive self-discharge in electrochemical energy storage devices is critical to improving device performance [138–140]. In doing so, elucidating the mechanisms driving layered cathode degradation in electrolytes and the impact on voltage fade and device lifetime can be better understood [141–143]. It has been previously reported that protons are available and can substitute on the Li^+ lattice site in $LiNiO_2$ and $LiCoO_2$ cathodes upon exposure to aqueous electrolytes or atmospheric moisture at high temperatures or high humidity [144–146]. A recent study by *Wan et al.* reveals that interfacial hydrogen transfer occurs from carbonate solvents to (de)lithiated nickel-manganese-cobalt oxide (NMC) cathodes[147], **Figure 9**.

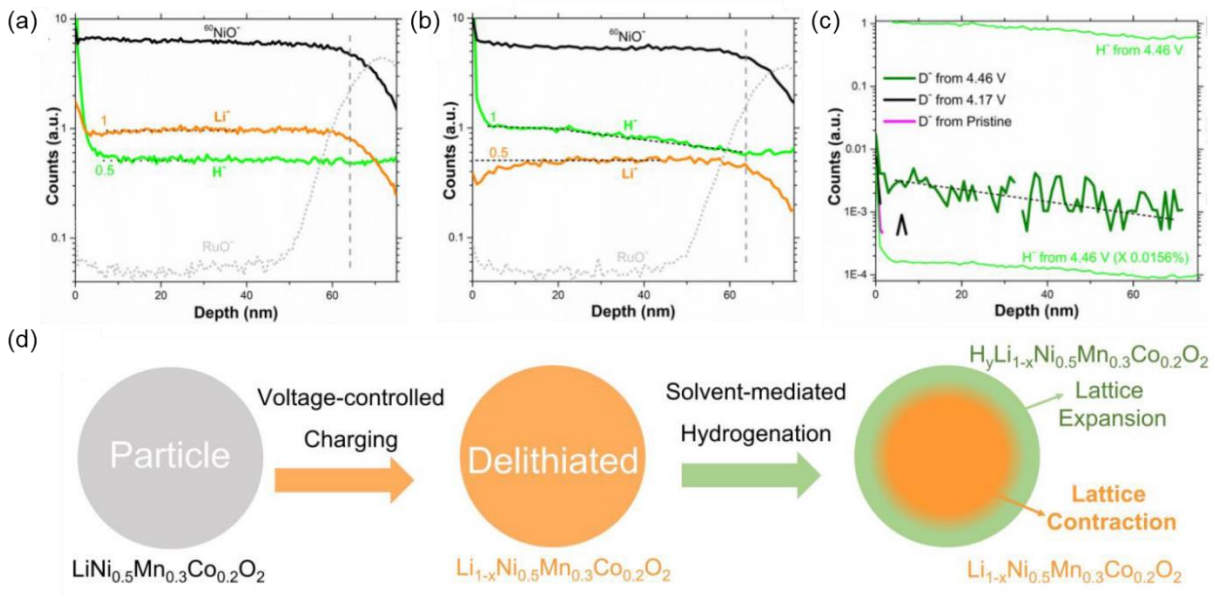

Figure 9: Using ToF-SIMS to analyze the cathode hydrogenation process. Depth profiles of the negative ions $^{60}NiO^-$, Li^-, H^-, and RuO^- from the (a) pristine $LiNi_xMn_yCo_{1-x-y}O_2$ (NMC) film grown on $SrRuO_3$ deposited on $SrTiO_3$ (110) substrate and (b) after self-discharge from an applied voltage of 4.46 V. (c) Potential-dependent depth profile of D^- and H^- signals for a pristine NMC film and after being exposed to deuterated electrolyte under a specified applied voltage. (d) ToF-SIMS depth profiling data suggest a mechanism of chemo-mechanical coupling in layered cathode particles, which involves both voltage-controlled delithiation (charging) and solvent-mediated hydrogenation[147].

Here, ToF-SIMS is employed to study a pristine NMC cathode, **Figure 9a**, and the subsequent hydrogenation after self-discharge during an applied voltage of 4.46 V, **Figure 9b**. The measurement reveals an enhancement of H^- signal upon self-discharge, suggesting an increase of protons within the NMC (~50% increase in the top 30 nm), and a subsequent decrease of an H-gradient, which is opposite to the Li gradient from the surface to the bulk, **Figure 9b**. Furthermore, a Li^- signal depletion within the first 20 nm of the NMC surface is seen, suggesting H and Li exchange during self-discharge [148]. To further confirm, isotopic labeling via a deuterated

electrolyte was used on the pristine sample and after self-discharge, and the D signal is shown to be above its natural abundance value after an applied voltage of 4.46 V, **Figure 9c**, thereby providing further evidence of solvent-mediated hydrogenation during the self-discharge process. In such a case, the unique high sensitivities of ToF-SIMS for both hydrogen and lithium demonstrates its valuable contribution to probing degradation mechanisms in lithium-ion battery systems and reiterates the importance of its use in depth-resolved analysis of diffusing species which dictate device performance.

2.2 Hydrogen imaging for spatial detection:

The submicron lateral resolutions and excellent depth resolution of ToF-SIMS can offer capabilities to directly detect and analyze H and its isotopes through spatially resolved 2D and 3D H imaging [27,46,149,150] to investigate localized hydrogen-induced property changes [27,46], glass corrosion [132,151,152] and many other interesting cases. During electrochemical H incorporation, when H-depth profiles in the films remain almost uniform throughout, the surface H concentrations can be altered by laterally varying surface voltages [26,27,32]. In such cases, the degree of local H-distribution across the surface becomes an obvious parameter to modulate its functional states, necessitating direct spatial H mapping, as indirect H-detection through the changes in lattices and altered electronic states would not be sufficient.

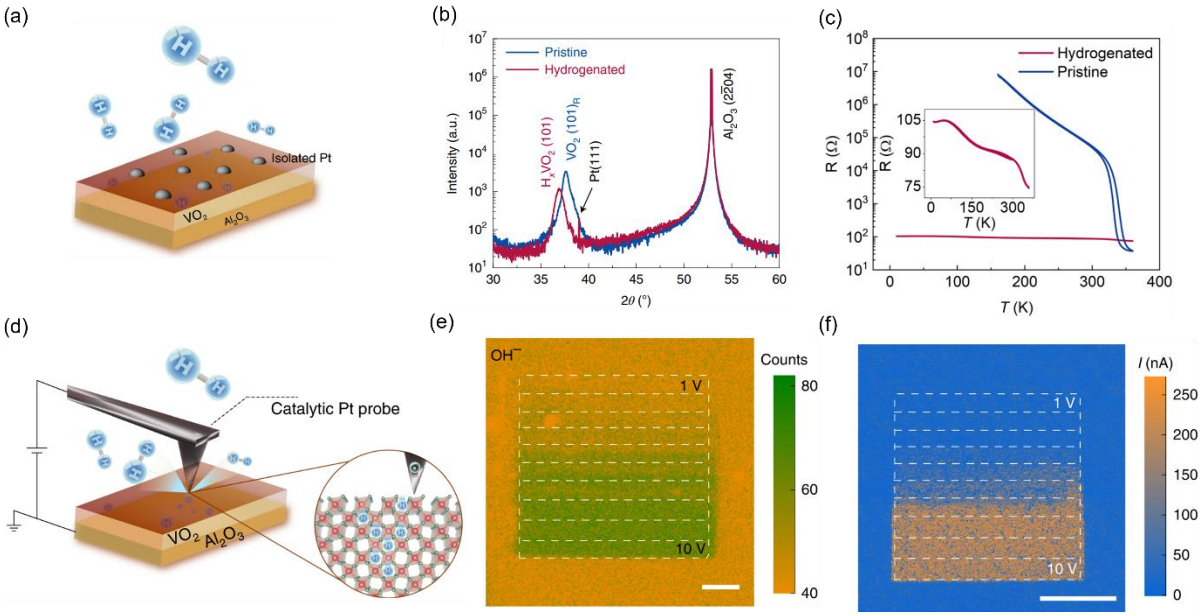

Figure 10: H imaging of the tip-induced H incorporation in VO_2 thin films. (a) hydrogen spillover via H_2 gas annealing and H dissociation on the film surface by Pt catalysts. (b) Hydrogenation-induced lattice modulations in VO_2 film. (c) Metal insulator transition from electrochemical H incorporation. (d) Pt-coated tip-induced electrochemical hydrogenation. (e) 2D ToF-SIMS H imaging shows a gradient of local H incorporation on the film surface due to spatially varied voltages from 1 to 10 V. (f) Spatial current mapping corresponding to the local H incorporation [27].

Figure 10 represents an example of the reversible electric field control of insulator-metal transition in VO_2 thin film by varying biasing voltages on the film surface. Efficient surface splitting and nanoscale incorporation of H were achieved via catalytic Pt-coating and tip voltage biasing from a Pt-probe across the surface, respectively, as shown in **Figure 10d**. The drivers of non-volatile switching of metallic and insulting states, achieved through positive and negative biasing tip voltages, were revealed by the ToF-SIMS imaging. The study observed that positive biasing leads to a hydrogenated metallic H_xVO_2 phase with an electrochemical H incorporation, while the

negative bias reversibly removes H reverting VO_2 into an insulating state. Notably, as seen in **Figure 10e**, increasing the positive biasing voltage shows an accelerated surface H-concentration and faster hydrogenation compared to other approaches [26,31], whereas lowering voltage leads to the lesser surface H. This potentially enables the modulation of switching speeds between the competing electronic states. While the previous examples shed light on depth-dependent H-incorporation to modulate electronic states in VO_2, ToF-SIMS imaging in this study captured voltage-induced spatial H-incorporation variation with similar depth profiles. This showcases ToF-SIMS as a critical technique to understand how inhomogeneous spatial H-incorporation potentially impacts the switching speed between the electronic states.

2.3 Direct isotopic analysis

Tritium-producing burnable absorber rods house the T breeder γ-$LiAlO_2$ in pressurized water reactors for T production [36]. A typical TPBAR consists of multiple concentric hollow tubes of zircaloy-4 liner, γ-$LiAlO_2$ pellets, nickel-plated zircaloy-4 T getter, and the outermost stainless-steel cladding, shown in **Figure 11a**. There are primarily two phenomena of interest for the functioning of the TPBARs in achieving optimum T retention. Firstly, the chemical reaction between T species and the metal getter, upon their release from pellets, forms metal hydrides. Secondly, the unwanted outward diffusion of T to the reactor coolant, and the inward diffusion of H from the reactor coolant to the T getter [153]. To address the latter, it is required to use an intermetallic coating as a diffusion barrier to minimize T permeation out of the TPBAR and H permeation into the TPBAR, **Figure 11a**. Thus, it is of utmost importance to examine the effects of irradiation on the performance of the intermetallic coating at an operating temperature of around 300 °C to understand gaseous diffusion of the chemical species within the TPBARs.

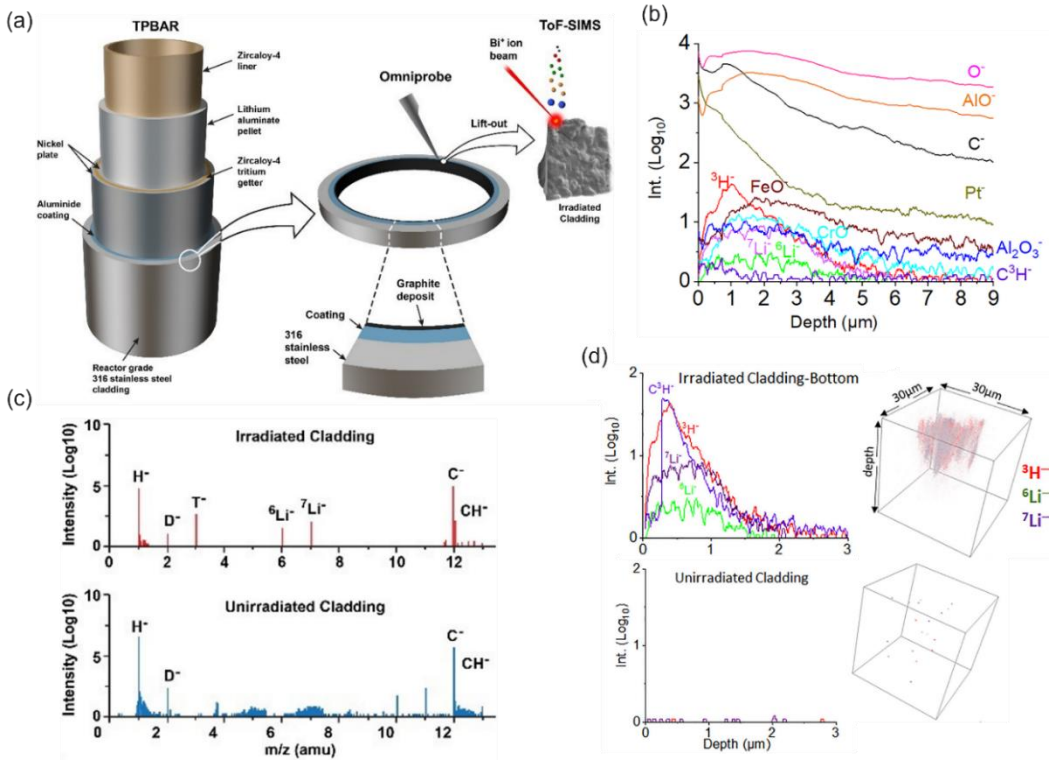

Figure 11: Schematic of TPBARs and direct detection of T from different modes of ToF-SIMS technique. (a) Section of the cladding with an aluminide layer for surface/depth analysis. (b) Depth profiling of the chemical species of interest, including T (^{3}H). (c) Direct detection of T in irradiated cladding via SIMS spectra. (d) The bottom portion of irradiated cladding shows the CT ($C^{3}H$) diffusion with H- and Li-isotopes[154].

The microscale understanding of irradiation-induced surface chemistry and structural changes, which lead to the deposition of the carbonaceous compounds and light isotopic distribution of T, ^{7}Li, and ^{6}Li on the aluminide coating barrier at the inner side of the stainless-steel cladding, was previously lacking. Due to its higher sensitivity for mapping H isotopes and light elements, ToF-SIMS was utilized to detect such deposited compounds and study the subsequent T and Li transport to the surface of the permeation barrier. The small sections of unirradiated and irradiated cladding samples with an aluminide layer were prepared and subjected to surface analysis, as

shown in **Figure 11a.** ToF-SIMS depth profiling of the irradiated sample in the negative ion mode reveals an apparent T diffusion up to 2 μm deep, along with the signatures of ^{7}Li, ^{6}Li, and carbonaceous cluster CT in the aluminide layer, **Figure 11b**. This is also corroborated by the direct detection of the elemental species of T, ^{7}Li, and ^{6}Li on the irradiated aluminide layer in its mass spectra, which are entirely absent on the spectra of the unirradiated layer, **Figure 11c.** The reconstructed 3D images from the depth profiling of the bottom part of the irradiated sample further supports an elemental and isotopic contrast between irradiated and unirradiated aluminide layers by tracking the diffusion of T, ^{7}Li, ^{6}Li, and CT species to the aluminide layer of the cladding during irradiation, as shown in **Figure 11d**.

The potential interference of ^{3}He during T detection can sometimes be a concern because T decays to form ^{3}He. Due to the minimal mass difference between T^- and $^{3}He^-$, it is difficult to distinguish them in ToF-SIMS spectra. However, since He is an inert gas, He^- yield is too low to be detected in SIMS [155]; therefore, $^{3}He^-$ interference is not an issue when analyzing T^- in SIMS.

More interestingly, combining deuterium isotopic labeling and ToF-SIMS depth or 2D/3D imaging analysis has been widely used to resolve many intriguing scientific questions[64,156–166]. A typical application is tracking mass transfer and chemical evolution of water and organic molecules in materials. For example, we used such a method to resolve a long-term debate about the original of the organic part of solid-electrolyte interphase in a Li metal battery[164].

3. Experimental Optimization

3.1 Sample preparation

Sample preparation is relatively simple for ToF-SIMS analysis. Generally, samples with flat surfaces are ideal as they can provide optimal signal intensity and mass resolution. SIMS signal can significantly drop at the edge of a sample (normally within 0.5 mm from the edge) due to uneven electric field[79]; therefore, there is a minimum sample size requirement (typically, 2×2 mm^2). The desirable sample sizes are 3×3 mm^2 to 12×12 mm^2 with various heights. Suppose the samples' size is indeed a limit. In that case, it is possible to put several small samples of the same type (same height) closely around the interesting sample to minimize the uneven electric field to achieve reasonable signal intensity. In addition, though SEM samples are normally acceptable for ToF-SIMS analysis, most of them may not be suitable for H analysis because the use of resin usually leads to poor vacuum and high H background. Therefore, reducing the use of resin is desirable, and if possible, resin-free sample mounting should be adopted.

3.2 Vacuum and hydrogen background

Reduction of H background when performing ToF-SIMS analysis is critical to improve detection limit and accurately determine H concentration within materials. The instrumental background is typically sourced from residual gaseous species that contain H, such as H_2, H_2O, and hydrocarbons. These residuals can adsorb on the sputter interface, leading to a higher equilibrium concentration of H during analysis. Therefore, pre-baking of the SIMS instrument and overnight pumping of samples in the introduction chamber are highly recommended to get a desirable vacuum for H analysis[79]. It should be noted that the ultimate base pressures of most SIMS analysis chambers are typically in the low 10^{-10} Torr range. Previous studies using magnetic SIMS have found that the partial pressure of H-containing molecules inside the chamber must be in the low 10^{-10} Torr range for a H background of ~ 0.01% (atomic ratio) during depth profiling [87,167] (Wang et al., 2007; Kudo et al., 2021). Recent ToF-SIMS work reports similar results, as < 0.01% (atomic ratio)

detection of H has been demonstrated[79,80], and the H background is roughly proportional to the pressure in the analysis chamber.

3.3 Hydrogen isotopic detection

A unique advantage of ToF-SIMS analysis is isotopic recognition capability. There are three isotopes of the element H: H, D, and T. Normally, negative ion analysis and non-interlaced mode dual beam depth profiling are used for D and T analysis because H_2^- and H_3^- interference signals are very low [154]. For example, in our ToF-SIMS analysis, H_2^- signal intensity is typically lower than the natural D^- (~ 1.5×10^{-4} of H^-) signal, and almost no H_3^- signal (less than 10^{-9} of H^-) is seen. Such an advantage makes the detection limit for D^- and T^- using ToF-SIMS around 1-10 ppm, 1-2 orders of magnitude better than that of H^-. As a comparison, in positive ion detection, H_2^+ and H_3^+ are relatively strong (typically 10^{-2} of H^+ for H_2^+ and 10^{-3} of H^+ for H_3^+ in our ToF-SIMS analysis), so D^+ and T^+ detection can be seriously interfered.

3.4 Polarity and sputter ions

Generally speaking, H^- is more sensitive than H^+ for ToF-SIMS detection [155]; therefore, negative ion depth profiling has been mainly used[79,155]. Another advantage of negative ion analysis is that the OH^- signal can be much stronger than the H^- signal in oxide samples, providing better data quality[27]. To enhance the number of negative ion signals during dual beam analysis, cesium (Cs^+) sputtering can be used as it is a strong electron donor[168]. However, H^+ sensitivity using an oxygen (O_2^+) sputtering beam is also acceptable[155]; therefore, positive ion detection can also be used, especially when simultaneous detection of metal ions is desirable. A typical example is the analysis of leached glass samples, in which the H and metallic ions need to be examined simultaneously to show the corrosion frontline[151,169]. However, due to increasing

vacuum pressure induced by O_2^+ gas (from the O_2^+ gun), the detection limit for H^+ depth profiling is around 0.2%-0.5% (atomic ratio).

3.5 Controlling surface charging during depth profiling

Another experimental parameter during ToF-SIMS depth profiling is operating in interlaced or non-interlaced mode. Interlaced mode utilizes the sputter ion beam between pulses from the analysis beam, such that both guns are operating quasi-simultaneously and quasi-continuously. Typically used for conductive and semi-conductive samples where charging is not an issue, maximal repetition rates along with optimum data rates and detection limits (e.g., 0.01% (atomic ratio) H background) can be achieved[79,166]. For insulating samples, an electron flood gun may not sufficiently compensate surface charging effects in interlaced mode, leading to low and unstable signals accompanied with poor mass resolution. In such a case, the non-interlaced mode can be used, where analysis phases are separated from the sputtering phases with a relaxation phase in between to reduce charging effects at the sample surface [166].

One big disadvantage of using a non-interlaced mode is the introduction of a high background of H, O, and C signals, as H_2, H_2O, CO, and CO_2 gas are typically highly present in vacuum chambers[79,170]. Studies on glass samples have shown that H background is around 1% (atomic ratio), thereby hindering its ability to track low concentrations of H signals[171].

A common way to minimize surface charging in ToF-SIMS analysis is the deposition of a thin (10-50 nm) gold layer on the sample surface. Though interlaced depth profiling of insulating samples may be effectively performed with such a gold coating layer to provide high-quality data, it can fail in many cases. Also, such a way introduces some surface contaminations and changes the surface's original state, which can be detrimental as the information of the surface's original

state may be important in many testing cases. We notice that the deposition of a thin gold layer at the back side of an insulating sample can also be very helpful in controlling surface charging. If the insulating sample can be thin (e.g., 0.5 mm or thinner), the back-side gold coating can be better than the front-side gold coating for charging control.

3.6 Cluster primary ion beam

While the introduction of cluster primary ion beams (i.e., Bi_n^+, C_{60}^{n+} or Ar_n^+) in ToF-SIMS analysis can greatly enhance the yield of secondary molecular ions, few advantages were observed in H analysis [95]. Previous work has shown that when compared to atomic primary ions with the same energy, cluster primary ions can enhance H^- and D^- ion yields, albeit very limited. Besides, one drawback of cluster ion beams is the lower currents that can be achieved in the currently available commercial ToF-SIMS instruments[170]. Therefore, monatomic ion beams may be the best choice for H depth profiling as they provide the highest effective signals and best detection limits for H^- and D^- compared to cluster ion beams.

3.7 Hydrogen quantification

H quantification using ToF-SIMS has been tricky due to the so-called matrix effect. The matrix effect is induced by various sputter yields and ionization yields (majorly, ionization yield differences that can vary in a range of several orders of magnitude) in different materials [101,102]. Therefore, a common way to quantify H in a sample is to prepare a reference in the same "matrix" with controllable H concentration, test the interesting samples and the reference using a ToF-SIMS instrument, and then normalize H signal to a matrix signal for a comparison to quantify the H concentration in the interesting samples. For example, a certain amount of H^+ can be implanted into a Si matrix and used as a reference sample to quantify H concentration in other Si samples[79]. The semiconductor industry has used such a way to quantify doped elements in Si and GaAs for

over 40 years[155]. However, in many scientific research cases, a good reference sample is not easily available, and semi-quantification, i.e., sample-to-sample comparison, is more important. Under such a situation, the absolute H concentrations can be estimated using relative sensitivity factors[155] of H and a matrix element. Though such an estimation is rough, the order of magnitude should be right. Indeed, such a strategy has been widely used[27,147].

3.8 Surface hydrocarbon contamination

It is a common issue that a thin layer (1-2 nm) of hydrocarbons can adsorb on the sample surface and remain even under high vacuum, leading to an observation of a strong H signal from the sample surface. Deleting the first one or several data spots in depth profiles is very common to minimize such an interference.

4. Summary and future prospects:

This review used representative examples to demonstrate how ToF-SIMS depth profiling and imaging can be utilized for H analysis in different materials, which have yielded deeper insights into materials, properties, processes, and chemistry. Of particular interest in such examples are the drivers of the electric field-induced electronic and magnetic states switching via electrolyte gating and hydrogen spillover in correlated oxide thin films and diffusion of H and/or its isotopes within γ-$LiAlO_2$ pellets in TPBARs used in fission reactors. As the surface and bulk H incorporation in materials cannot be directly detected by routine analytical techniques like TEM, XPS, etc., the key material challenges showcased through the examples have informed an urgent need for ToF-SIMS because of its unique capabilities for nanoscale H detection. It should be noted that there are certain protocols and good practices in sample preparation and parameter selection to enhance the H-detection limit, as summarized in the previous section, and they are intended to be used as guidance

for researchers when planning to utilize ToF-SIMS. Moreover, other complementary techniques including APT, ERDA, and NRA can be synergistically utilized with ToF-SIMS to acquire complementary information.

Among the future directions toward H detection via ToF-SIMS is using cryogenic conditions during analysis. Normally, ToF-SIMS depth profiling is performed at room temperature. However, during depth profiling testing, some energy can be transferred from the sputter ions onto the sputter interface, and such energy may induce H motion if the H atoms are loosely bonded in the sample (such as H atoms in metals). A typical example is ToF-SIMS depth profiling of implanted H in Nb metal [61], where cooling the Nb metal to liquid N_2 temperature can significantly reduce H motion. Indeed, low-temperature analysis has been used in traditional magnetic SIMS depth profiling of H for a long time [174–176].

Nevertheless, ToF-SIMS investigation of H in materials has been gaining significant interest, and the need to address several outstanding materials challenges warrants the enablement of advanced detection approaches. These include lowering down the background H, suppressing its diffusion, and performing in-situ detection during the isotope exchanges. Hydrogenation-driven phenomena hitherto studied are narrow and limited to specific strongly correlated oxides that are extremely responsive to H. Investigation of H-incorporation-property relationships in oxides that are less sensitive to H by utilizing advanced detection modes and techniques can unleash additional functional states. Towards the discovery of emergent properties, an uncharted territory exists to exploit H as a powerful knob to realize unprecedented properties. Given that materials-based H storage is receiving a great deal of attention because of the higher storage density and safety concerns associated with physical storage, understanding the mobility and dynamics of interstitial H within the host compound is of prime importance. In light of these, ToF-SIMS will remain the

technique for state-of-the-art nanoscale H analysis where higher sensitivity, direct H detection, facile sample preparation, and high throughput analysis are desirable.

Data availability

No data was used for the research described in the article.

Declaration of Competing Interest

The authors declare that they have no known competing financial interests or personal relationships that could have appeared to influence the work reported in this paper.

Acknowledgements

The work was supported by the U.S. Department of Energy (DOE), Office of Science, Office of Basic Energy Sciences, under award #10122. Work on tritium detection was supported by the Tritium Modernization Program of the DOE's National Nuclear Security Administration. A portion of this work was performed in the W. R. Wiley Environmental Molecular Sciences Laboratory, a national scientific user facility sponsored by the DOE located at the Pacific Northwest National Laboratory (PNNL). PNNL is operated by Battelle under the contract DE-AC05-76RL01830.

References:

[1] K. Way, L. Fano, M.R. Scott, K. Thew, Circular of the Bureau of Standards No. 499:: Nuclear Data- a Collection of Experimental Values of Half-Lives, Radiation Energies, Relative Isotopic Abundances, Nuclear Moments, and Cross Sections, National Bureau of Standards, Gaithersburg, MD, 1950.
[2] F. Ueckerdt, C. Bauer, A. Dirnaichner, J. Everall, R. Sacchi, G. Luderer, Nat. Clim. Chang. 11 (2021) 384–393.
[3] I. Staffell, D. Scamman, A. Velazquez Abad, P. Balcombe, P.E. Dodds, P. Ekins, N. Shah, K.R. Ward, Energy Environ. Sci. 12 (2019) 463–491.
[4] M.D. Allendorf, Z. Hulvey, T. Gennett, A. Ahmed, T. Autrey, J. Camp, E. Seon Cho, H. Furukawa, M. Haranczyk, M. Head-Gordon, S. Jeong, A. Karkamkar, D.-J. Liu, J.R. Long, K.R. Meihaus, I.H. Nayyar, R. Nazarov, D.J. Siegel, V. Stavila, J.J. Urban, S.P. Veccham, B.C. Wood, Energy Environ. Sci. 11 (2018) 2784–2812.
[5] S.E. Hosseini, M.A. Wahid, Renewable and Sustainable Energy Reviews 57 (2016) 850–866.
[6] K.D. Kreuer, Annu. Rev. Mater. Res. 33 (2003) 333–359.
[7] C.G. Van de Walle, J. Neugebauer, Annu. Rev. Mater. Res. 36 (2006) 179–198.
[8] S.M. Myers, M.I. Baskes, H.K. Birnbaum, J.W. Corbett, G.G. DeLeo, S.K. Estreicher, E.E. Haller, P. Jena, N.M. Johnson, R. Kirchheim, S.J. Pearton, M.J. Stavola, Rev. Mod. Phys. 64 (1992) 559–617.
[9] W. Beyer, Phys. Status Solidi A 213 (2016) 1661–1674.
[10] M. Morales-Masis, L. Ding, F. Dauzou, Q. Jeangros, A. Hessler-Wyser, S. Nicolay, C. Ballif, APL Materials 2 (2014) 096113.
[11] T. Nagashima, M. Koyama, A. Bashir, M. Rohwerder, C.C. Tasan, E. Akiyama, D. Raabe, K. Tsuzaki, Materials and Corrosion 68 (2017) 306–310.
[12] J.H. Ryu, S.K. Kim, C.S. Lee, D.-W. Suh, H.K.D.H. Bhadeshia, Proc. R. Soc. A. 469 (2013) 20120458.
[13] M. Lozada-Hidalgo, S. Hu, O. Marshall, A. Mishchenko, A.N. Grigorenko, R.A.W. Dryfe, B. Radha, I.V. Grigorieva, A.K. Geim, Science 351 (2016) 68–70.
[14] D.R. Augood, Nature 178 (1956) 754–755.
[15] G. McMahon, B.D. Miller, M.G. Burke, Npj Mater Degrad 2 (2018) 2.
[16] S. Kohiki, M. Nishitani, T. Wada, T. Hirao, Appl. Phys. Lett. 64 (1994) 2876–2878.
[17] E.V. Monakhov, J.S. Christensen, K. Maknys, B.G. Svensson, A.Yu. Kuznetsov, Appl. Phys. Lett. 87 (2005) 191910.
[18] T. Asakawa, D. Nagano, S. Denda, K. Miyairi, Jpn. J. Appl. Phys. 47 (2008) 649–652.
[19] N. Chantarat, S.-H. Hsu, C.-C. Lin, M.-C. Chiang, S.-Y. Chen, J. Mater. Chem. 22 (2012) 8005.
[20] K. Nomura, T. Kamiya, H. Hosono, ECS J. Solid State Sci. Technol. 2 (2013) P5–P8.
[21] D. Gaspar, L. Pereira, K. Gehrke, B. Galler, E. Fortunato, R. Martins, Solar Energy Materials and Solar Cells 163 (2017) 255–262.
[22] Z. Li, Y. Lyu, Z. Ran, Y. Wang, Y. Zhang, N. Lu, M. Wang, M. Sassi, T.D. Ha, A. T. N'Diaye, P. Shafer, C. Pearce, K. Rosso, E. Arenholz, J. Juang, Q. He, Y. Chu, W. Luo, P. Yu, Adv Funct Materials 33 (2023) 2212298.
[23] H. Jani, J. Linghu, S. Hooda, R.V. Chopdekar, C. Li, G.J. Omar, S. Prakash, Y. Du, P. Yang, A. Banas, K. Banas, S. Ghosh, S. Ojha, G.R. Umapathy, D. Kanjilal, A. Ariando, S.J. Pennycook, E. Arenholz, P.G. Radaelli, J.M.D. Coey, Y.P. Feng, T. Venkatesan, Nat Commun 12 (2021) 1668.
[24] J. Shi, Y. Zhou, S. Ramanathan, Nat Commun 5 (2014) 4860.
[25] K. Shibuya, A. Sawa, Adv. Electron. Mater. 2 (2016) 1500131.
[26] N. Lu, P. Zhang, Q. Zhang, R. Qiao, Q. He, H.-B. Li, Y. Wang, J. Guo, D. Zhang, Z. Duan, Z. Li, M. Wang, S. Yang, M. Yan, E. Arenholz, S. Zhou, W. Yang, L. Gu, C.-W. Nan, J. Wu, Y. Tokura, P. Yu, Nature 546 (2017) 124–128.
[27] L. Li, M. Wang, Y. Zhou, Y. Zhang, F. Zhang, Y. Wu, Y. Wang, Y. Lyu, N. Lu, G. Wang, H. Peng, S. Shen, Y. Du, Z. Zhu, C.-W. Nan, P. Yu, Nat. Mater. (2022).

[28] N. Lu, Z. Zhang, Y. Wang, H.-B. Li, S. Qiao, B. Zhao, Q. He, S. Lu, C. Li, Y. Wu, M. Zhu, X. Lyu, X. Chen, Z. Li, M. Wang, J. Zhang, S.C. Tsang, J. Guo, S. Yang, J. Zhang, K. Deng, D. Zhang, J. Ma, J. Ren, Y. Wu, J. Zhu, S. Zhou, Y. Tokura, C.-W. Nan, J. Wu, P. Yu, Nat Energy 7 (2022) 1208–1216.
[29] S.G. Altendorf, J. Jeong, D. Passarello, N.B. Aetukuri, M.G. Samant, S.S.P. Parkin, Adv. Mater. 28 (2016) 5284–5292.
[30] F. Zhang, Y. Zhang, L. Li, X. Mou, H. Peng, S. Shen, M. Wang, K. Xiao, S.-H. Ji, D. Yi, T. Nan, J. Tang, P. Yu, Nat Commun 14 (2023) 3950.
[31] H. Yoon, M. Choi, T.-W. Lim, H. Kwon, K. Ihm, J.K. Kim, S.-Y. Choi, J. Son, Nature Mater 15 (2016) 1113–1119.
[32] H. Chen, M. Dong, Y. Hu, T. Lin, Q. Zhang, E.-J. Guo, L. Gu, J. Wu, Q. Lu, Nano Lett. 22 (2022) 8983–8990.
[33] Y.J. Li, T.C. Kaspar, T.C. Droubay, Z. Zhu, V. Shutthanandan, P. Nachimuthu, S.A. Chambers, Appl. Phys. Lett. 92 (2008) 152105.
[34] H. Nakaya, H. Matsuura, Y. Nakao, S. Shimakawa, M. Goto, S. Nakagawa, M. Nishikawa, Nuclear Engineering and Design 271 (2014) 505–509.
[35] H.P. Paudel, Y.-L. Lee, D.J. Senor, Y. Duan, J. Phys. Chem. C 122 (2018) 9755–9765.
[36] D.J. Senor, Science and Technology in Support of the Tritium Modernization Program, 2021.
[37] W. Jiang, J. Zhang, L. Kovarik, Z. Zhu, L. Price, J. Gigax, E. Castanon, X. Wang, L. Shao, D.J. Senor, Journal of Nuclear Materials 484 (2017) 374–381.
[38] C.M. Jantzen, Journal of Non-Crystalline Solids 84 (1986) 215–225.
[39] W. Lutze, G. Malow, R.C. Ewing, M.J. Jercinovic, K. Keil, Nature 314 (1985) 252–255.
[40] C.M. Jantzen, M.J. Plodinec, Journal of Non-Crystalline Solids 67 (1984) 207–223.
[41] B. Grambow, MRS Proc. 44 (1984) 15.
[42] S. Gin, P. Jollivet, G. Barba Rossa, M. Tribet, S. Mougnaud, M. Collin, M. Fournier, E. Cadel, M. Cabie, L. Dupuy, Geochimica et Cosmochimica Acta 202 (2017) 57–76.
[43] M. Collin, S. Gin, P. Jollivet, L. Dupuy, V. Dauvois, L. Duffours, Npj Mater Degrad 3 (2019) 14.
[44] M. Kawai, S. Inoue, M. Mizumaki, N. Kawamura, N. Ichikawa, Y. Shimakawa, Applied Physics Letters 94 (2009) 082102.
[45] P. Puphal, Y.-M. Wu, K. Fürsich, H. Lee, M. Pakdaman, J.A.N. Bruin, J. Nuss, Y.E. Suyolcu, P.A. van Aken, B. Keimer, M. Isobe, M. Hepting, Sci. Adv. 7 (2021) eabl8091.
[46] X. Ding, C.C. Tam, X. Sui, Y. Zhao, M. Xu, J. Choi, H. Leng, J. Zhang, M. Wu, H. Xiao, X. Zu, M. Garcia-Fernandez, S. Agrestini, X. Wu, Q. Wang, P. Gao, S. Li, B. Huang, K.-J. Zhou, L. Qiao, Nature 615 (2023) 50–55.
[47] D. Li, K. Lee, B.Y. Wang, M. Osada, S. Crossley, H.R. Lee, Y. Cui, Y. Hikita, H.Y. Hwang, Nature 572 (2019) 624–627.
[48] T. Katayama, A. Chikamatsu, K. Yamada, K. Shigematsu, T. Onozuka, M. Minohara, H. Kumigashira, E. Ikenaga, T. Hasegawa, J. Appl. Phys. 120 (2016) 085305.
[49] L. Si, W. Xiao, J. Kaufmann, J.M. Tomczak, Y. Lu, Z. Zhong, K. Held, Phys. Rev. Lett. 124 (2020) 166402.
[50] A.A. Murthy, J. Lee, C. Kopas, M.J. Reagor, A.P. McFadden, D.P. Pappas, M. Checchin, A. Grassellino, A. Romanenko, Appl. Phys. Lett. 120 (2022) 044002.
[51] H. Deng, L. Zhao, K. Park, J. Yan, K. Sobczak, A. Lakra, E. Buzi, L. Krusin-Elbaum, Nat Commun 13 (2022) 2308.
[52] S. Dekura, H. Kobayashi, K. Kusada, H. Kitagawa, ChemPhysChem 20 (2019) 1158–1176.
[53] M.T. Brumbach, J.A. Ohlhausen, K.R. Zavadil, C.S. Snow, J.C. Woicik, Journal of Applied Physics 109 (2011) 114911.
[54] R.R. Wixom, J.F. Browning, C.S. Snow, P.A. Schultz, D.R. Jennison, Journal of Applied Physics 103 (2008) 123708.

[55] S. Orimo, Y. Nakamori, J.R. Eliseo, A. Züttel, C.M. Jensen, Chem. Rev. 107 (2007) 4111–4132.
[56] L.J. Murray, M. Dincă, J.R. Long, Chem. Soc. Rev. 38 (2009) 1294.
[57] D.A. Lawrenz, J. Mitchell, in: R.A. Meyers (Ed.), Encyclopedia of Analytical Chemistry, John Wiley & Sons, Ltd, Chichester, UK, 2006, p. a2414.
[58] E. Tal-Gutelmacher, D. Eliezer, E. Abramov, Materials Science and Engineering: A 445–446 (2007) 625–631.
[59] Z. Weiss, Hydrogen 2 (2021) 225–245.
[60] P. Maheshwari, F.A. Stevie, G. Myeneni, G. Ciovati, J.M. Rigsbee, D.P. Griffis, in: Virginia, (USA), 2011, pp. 151–160.
[61] F.A. Stevie, Surf. Interface Anal. 48 (2016) 310–314.
[62] H. Takahara, R. Ishigami, K. Kodama, A. Kojyo, T. Nakamura, Y. Oka, J. Anal. At. Spectrom. 31 (2016) 940–947.
[63] J. Steffens, H.-W. Becker, S. Gerke, S. Joos, G. Hahn, B. Terheiden, Energy Procedia 124 (2017) 180–187.
[64] X. Wu, A. Seyeux, I. Vickridge, S. Voyshnis, P. Marcus, Corrosion Science 140 (2018) 151–158.
[65] P. Paris, I. Jõgi, K. Piip, M. Passoni, D. Dellasega, E. Grigore, W.M. Arnoldbik, H. van der Meiden, Fusion Engineering and Design 168 (2021) 112403.
[66] D.D. Cohen, R. Bird, N. Dytlewski, R. Siegele, in: Encyclopedia of Physical Science and Technology, Elsevier, 2003, pp. 55–63.
[67] T.S. Wang, D. Grambole, F. Herrmann, H.B. Peng, S.W. Wang, Surf. Interface Anal. 39 (2007) 52–57.
[68] M. Wilde, K. Fukutani, Surface Science Reports 69 (2014) 196–295.
[69] H. Kudo, H. Naramoto, M. Sataka, S. Ishii, K. Sasa, S. Tomita, J. Phys.: Condens. Matter 33 (2021) 465901.
[70] J. Takahashi, K. Kawakami, H. Otsuka, H. Fujii, Ultramicroscopy 109 (2009) 568–573.
[71] J. Takahashi, K. Kawakami, Y. Kobayashi, T. Tarui, Scripta Materialia 63 (2010) 261–264.
[72] A.J. Breen, L.T. Stephenson, B. Sun, Y. Li, O. Kasian, D. Raabe, M. Herbig, B. Gault, Acta Materialia 188 (2020) 108–120.
[73] Y.-S. Chen, H. Lu, J. Liang, A. Rosenthal, H. Liu, G. Sneddon, I. McCarroll, Z. Zhao, W. Li, A. Guo, J.M. Cairney, Science 367 (2020) 171–175.
[74] A. Devaraj, B. Matthews, B. Arey, L. Bagaasen, E. Buck, G. Sevigny, D. Senor, Materials Characterization 176 (2021) 111095.
[75] S.-I. Baik, L. Ma, Y.-J. Kim, B. Li, M. Liu, D. Isheim, B.I. Yakobson, P.M. Ajayan, D.N. Seidman, Small 11 (2015) 5968–5974.
[76] G. Sundell, M. Thuvander, H.-O. Andrén, Ultramicroscopy 132 (2013) 285–289.
[77] P. Felfer, B. Ott, M. Monajem, V. Dalbauer, M. Heller, J. Josten, C. Macaulay, Microsc Microanal 28 (2022) 1255–1263.
[78] Y. Chang, W. Lu, J. Guénolé, L.T. Stephenson, A. Szczpaniak, P. Kontis, A.K. Ackerman, F.F. Dear, I. Mouton, X. Zhong, S. Zhang, D. Dye, C.H. Liebscher, D. Ponge, S. Korte-Kerzel, D. Raabe, B. Gault, Nat Commun 10 (2019) 942.
[79] Z. Zhu, V. Shutthanandan, M. Engelhard, Surf. Interface Anal. 44 (2012) 232–237.
[80] F.A. Stevie, C. Zhou, M. Hopstaken, M. Saccomanno, Z. Zhang, A. Turansky, Journal of Vacuum Science & Technology B, Nanotechnology and Microelectronics: Materials, Processing, Measurement, and Phenomena 34 (2016) 03H103.
[81] K.L. Moore, E. Lombi, F.-J. Zhao, C.R.M. Grovenor, Anal Bioanal Chem 402 (2012) 3263–3273.
[82] P. Hoppe, S. Cohen, A. Meibom, Geostand Geoanal Res 37 (2013) 111–154.
[83] D. Huang, X. Hua, G.-L. Xiu, Y.-J. Zheng, X.-Y. Yu, Y.-T. Long, Analytica Chimica Acta 989 (2017) 1–14.
[84] B.L. Gorman, M.L. Kraft, Anal. Chem. 92 (2020) 1645–1652.

[85] J.L. Mosenfelder, M. Le Voyer, G.R. Rossman, Y. Guan, D.R. Bell, P.D. Asimow, J.M. Eiler, American Mineralogist 96 (2011) 1725–1741.
[86] K. Koga, E. Hauri, M. Hirschmann, D. Bell, Geochem. Geophys. Geosyst. 4 (2003).
[87] C.W. Magee, E.M. Botnick, Journal of Vacuum Science and Technology 19 (1981) 47–52.
[88] M. Koyama, M. Rohwerder, C.C. Tasan, A. Bashir, E. Akiyama, K. Takai, D. Raabe, K. Tsuzaki, Materials Science and Technology 33 (2017) 1481–1496.
[89] A. Benninghoven, Angew. Chem. Int. Ed. Engl. 33 (1994) 1023–1043.
[90] R.N.S. Sodhi, Analyst 129 (2004) 483–487.
[91] A. Brown, J.C. Vickerman, Surf. Interface Anal. 6 (1984) 1–14.
[92] J.C. Vickerman, D. Briggs, SurfaceSpectra Ltd, eds., ToF-SIMS: Surface Analysis by Mass Spectrometry, IM, Chichester, 2001.
[93] J.C. Vickerman, D. Briggs, eds., ToF-SIMS: Materials Analysis by Mass Spectrometry, 2nd edition, SurfaceSpectra Limited, Manchester, 2013.
[94] A.M. Spool, The Practice of TOF-SIMS: Time of Flight Secondary Ion Mass Spectrometry, Momentum Press, LLC, New York, 2016.
[95] N. Winograd, Anal. Chem. 77 (2005) 142 A-149 A.
[96] Z. Wang, B. Liu, E.W. Zhao, K. Jin, Y. Du, J.J. Neeway, J.V. Ryan, D. Hu, K.H.L. Zhang, M. Hong, S. Le Guernic, S. Thevuthasan, F. Wang, Z. Zhu, J. Am. Soc. Mass Spectrom. 26 (2015) 1283–1290.
[97] M. Wang, S. Shen, J. Ni, N. Lu, Z. Li, H. Li, S. Yang, T. Chen, J. Guo, Y. Wang, H. Xiang, P. Yu, Adv. Mater. 29 (2017) 1703628.
[98] H. Li, F. Lou, Y. Wang, Y. Zhang, Q. Zhang, D. Wu, Z. Li, M. Wang, T. Huang, Y. Lyu, J. Guo, T. Chen, Y. Wu, E. Arenholz, N. Lu, N. Wang, Q. He, L. Gu, J. Zhu, C. Nan, X. Zhong, H. Xiang, P. Yu, Adv. Sci. 6 (2019) 1901432.
[99] D. Yi, Y. Wang, O.M.J. van 't Erve, L. Xu, H. Yuan, M.J. Veit, P.P. Balakrishnan, Y. Choi, A.T. N'Diaye, P. Shafer, E. Arenholz, A. Grutter, H. Xu, P. Yu, B.T. Jonker, Y. Suzuki, Nat Commun 11 (2020) 902.
[100] Z. Li, S. Shen, Z. Tian, K. Hwangbo, M. Wang, Y. Wang, F.M. Bartram, L. He, Y. Lyu, Y. Dong, G. Wan, H. Li, N. Lu, J. Zang, H. Zhou, E. Arenholz, Q. He, L. Yang, W. Luo, P. Yu, Nat Commun 11 (2020) 184.
[101] S. Chen, Z. Wang, H. Ren, Y. Chen, W. Yan, C. Wang, B. Li, J. Jiang, C. Zou, Sci. Adv. 5 (2019) eaav6815.
[102] P.A. Sermon, G.C. Bond, Catalysis Reviews 8 (1974) 211–239.
[103] H. Han, H. Zhou, C. Guillemard, M. Valvidares, A. Sharma, Y. Li, A.K. Sharma, I. Kostanovskiy, A. Ernst, S.S.P. Parkin, Advanced Materials 35 (2023) 2207246.
[104] Y. Zhou, X. Guan, H. Zhou, K. Ramadoss, S. Adam, H. Liu, S. Lee, J. Shi, M. Tsuchiya, D.D. Fong, S. Ramanathan, Nature 534 (2016) 231–234.
[105] D.A. Panayotov, J.T. Yates, J. Phys. Chem. C 111 (2007) 2959–2964.
[106] J. Wei, H. Ji, W. Guo, A.H. Nevidomskyy, D. Natelson, Nature Nanotech 7 (2012) 357–362.
[107] Y. Chen, Z. Wang, S. Chen, H. Ren, L. Wang, G. Zhang, Y. Lu, J. Jiang, C. Zou, Y. Luo, Nat Commun 9 (2018) 818.
[108] Q. Zhu, S. Jiang, K. Ye, W. Hu, J. Zhang, X. Niu, Y. Lin, S. Chen, L. Song, Q. Zhang, J. Jiang, Y. Luo, Adv. Mater. 32 (2020) 2004059.
[109] L. Xie, Q. Zhu, G. Zhang, K. Ye, C. Zou, O.V. Prezhdo, Z. Wang, Y. Luo, J. Jiang, J. Am. Chem. Soc. 142 (2020) 4136–4140.
[110] I.A. Zaluzhnyy, P.O. Sprau, R. Tran, Q. Wang, H.-T. Zhang, Z. Zhang, T.J. Park, N. Hua, B. Stoychev, M.J. Cherukara, M.V. Holt, E. Nazaretski, X. Huang, H. Yan, A. Pattammattel, Y.S. Chu, S.P. Ong, S. Ramanathan, O.G. Shpyrko, A. Frano, Phys. Rev. Materials 5 (2021) 095003.
[111] L. Gao, H. Wang, F. Meng, H. Peng, X. Lyu, M. Zhu, Y. Wang, C. Lu, J. Liu, T. Lin, A. Ji, Q. Zhang, L. Gu, P. Yu, S. Meng, Z. Cao, N. Lu, Advanced Materials 35 (2023) 2300617.

[112] Z. Zhang, D. Schwanz, B. Narayanan, M. Kotiuga, J.A. Dura, M. Cherukara, H. Zhou, J.W. Freeland, J. Li, R. Sutarto, F. He, C. Wu, J. Zhu, Y. Sun, K. Ramadoss, S.S. Nonnenmann, N. Yu, R. Comin, K.M. Rabe, S.K.R.S. Sankaranarayanan, S. Ramanathan, Nature 553 (2018) 68–72.
[113] J. Chen, W. Mao, B. Ge, J. Wang, X. Ke, V. Wang, Y. Wang, M. Döbeli, W. Geng, H. Matsuzaki, J. Shi, Y. Jiang, Nat Commun 10 (2019) 694.
[114] J. Park, H. Yoon, H. Sim, S.-Y. Choi, J. Son, ACS Nano 14 (2020) 2533–2541.
[115] S. Seo, J.-G. Yoon, J.D. Kim, T.K. Song, B.S. Kang, T.W. Noh, Y.K. Lee, Ch.J. Kim, I.S. Lee, J.K. Lee, Y.S. Park, Appl. Phys. Lett. 81 (2002) 1857–1859.
[116] Y. Takada, N. Okamoto, T. Saito, T. Yoshimura, N. Fujimura, K. Higuchi, A. Kitajima, R. Shishido, IEEE Trans. Ultrason., Ferroelect., Freq. Contr. 63 (2016) 1668–1673.
[117] C. Müller, J.H. Cole, J. Lisenfeld, Rep. Prog. Phys. 82 (2019) 124501.
[118] M. Kjaergaard, M.E. Schwartz, J. Braumüller, P. Krantz, J.I.-J. Wang, S. Gustavsson, W.D. Oliver, Annu. Rev. Condens. Matter Phys. 11 (2020) 369–395.
[119] A. Romanenko, R. Pilipenko, S. Zorzetti, D. Frolov, M. Awida, S. Belomestnykh, S. Posen, A. Grassellino, Phys. Rev. Applied 13 (2020) 034032.
[120] P. Puphal, V. Pomjakushin, R.A. Ortiz, S. Hammoud, M. Isobe, B. Keimer, M. Hepting, Front. Phys. 10 (2022) 842578.
[121] W. Jiang, J. Zhang, D.J. Edwards, N.R. Overman, Z. Zhu, L. Price, J. Gigax, E. Castanon, L. Shao, D.J. Senor, Journal of Nuclear Materials 494 (2017) 411–421.
[122] W. Jiang, T. Wang, Y. Wang, Z. Zhu, L. Shao, D.J. Senor, Journal of Nuclear Materials 538 (2020) 152357.
[123] W. Jiang, W.G. Luscher, T. Wang, Z. Zhu, L. Shao, D.J. Senor, Journal of Nuclear Materials 542 (2020) 152532.
[124] P. Van Iseghem, M. Aertsens, K. Lemmens, S. Gin, D. Deneele, B. Grambow, P. McGrail, D. Strachan, G. Wicks, T. McMenamin, A Critical Evaluation of the Dissolution Mechanisms of High Level Waste Glasses in Conditions of Relevance for Geological Disposal, 2005.
[125] S. Gin, A. Abdelouas, L.J. Criscenti, W.L. Ebert, K. Ferrand, T. Geisler, M.T. Harrison, Y. Inagaki, S. Mitsui, K.T. Mueller, J.C. Marra, C.G. Pantano, E.M. Pierce, J.V. Ryan, J.M. Schofield, C.I. Steefel, J.D. Vienna, Materials Today 16 (2013) 243–248.
[126] M.I. Ojovan, An Introduction to Nuclear Waste Immobilisation / Michael I. Ojovan, William E. Lee, Stepan N. Kalmykov, Third Edition, Elsevier, Amsterdam, 2019.
[127] B.A. Pulsipher, High-Level Waste Qualification: Managing Uncertainty, USA, 1982.
[128] B. Grambow, Elements 2 (2006) 357–364.
[129] S. Gin, C. Jegou, L. Sessegolo, N. Bisbrouck, A. Jan, M. Tribet, J.M. Delaye, F. Angeli, Npj Mater Degrad 6 (2022) 59.
[130] K. Damodaran, S. Gin, S. Naranayasamy, J.-M. Delaye, Npj Mater Degrad 7 (2023) 46.
[131] T. Chave, P. Frugier, S. Gin, A. Ayral, Geochimica et Cosmochimica Acta 75 (2011) 4125–4139.
[132] S. Gin, P. Jollivet, M. Fournier, C. Berthon, Z. Wang, A. Mitroshkov, Z. Zhu, J.V. Ryan, Geochimica et Cosmochimica Acta 151 (2015) 68–85.
[133] H. Zhang, T. Suzuki-Muresan, S. Gin, G. Blain, T. Sauvage, O. Wendling, J. Vandenborre, A. Abdelouas, Journal of Nuclear Materials 578 (2023) 154368.
[134] C. Cailleteau, F. Angeli, F. Devreux, S. Gin, J. Jestin, P. Jollivet, O. Spalla, Nature Mater 7 (2008) 978–983.
[135] R. Hellmann, S. Cotte, E. Cadel, S. Malladi, L.S. Karlsson, S. Lozano-Perez, M. Cabié, A. Seyeux, Nature Mater 14 (2015) 307–311.
[136] T. Geisler, A. Janssen, D. Scheiter, T. Stephan, J. Berndt, A. Putnis, Journal of Non-Crystalline Solids 356 (2010) 1458–1465.
[137] S. Gin, P. Jollivet, M. Fournier, F. Angeli, P. Frugier, T. Charpentier, Nat Commun 6 (2015) 6360.

[138] K. Xu, Chem. Rev. 104 (2004) 4303–4418.
[139] D.S. Hall, T. Hynes, J.R. Dahn, J. Electrochem. Soc. 165 (2018) A2961–A2967.
[140] H.A. Andreas, J. Electrochem. Soc. 162 (2015) A5047–A5053.
[141] J.P. Pender, G. Jha, D.H. Youn, J.M. Ziegler, I. Andoni, E.J. Choi, A. Heller, B.S. Dunn, P.S. Weiss, R.M. Penner, C.B. Mullins, ACS Nano 14 (2020) 1243–1295.
[142] R. Hausbrand, G. Cherkashinin, H. Ehrenberg, M. Gröting, K. Albe, C. Hess, W. Jaegermann, Materials Science and Engineering: B 192 (2015) 3–25.
[143] M. Jiang, D.L. Danilov, R. Eichel, P.H.L. Notten, Advanced Energy Materials 11 (2021) 2103005.
[144] T. Toma, R. Maezono, K. Hongo, ACS Appl. Energy Mater. 3 (2020) 4078–4087.
[145] S. Posada-Pérez, G.-M. Rignanese, G. Hautier, Chem. Mater. 33 (2021) 6942–6954.
[146] L. Hartmann, D. Pritzl, H. Beyer, H.A. Gasteiger, J. Electrochem. Soc. 168 (2021) 070507.
[147] G. Wan, T.P. Pollard, L. Ma, M.A. Schroeder, C.-C. Chen, Z. Zhu, Z. Zhang, C.-J. Sun, J. Cai, H.L. Thaman, A. Vailionis, H. Li, S. Kelly, Z. Feng, J. Franklin, S.P. Harvey, Y. Zhang, Y. Du, Z. Chen, C.J. Tassane, H.-G. Steinrück, K. Xu, O. Borodin, M.F. Toney, Science (under final revision) (2023).
[148] L. Dörrer, R. Heller, H. Schmidt, Phys. Chem. Chem. Phys. 24 (2022) 16139–16147.
[149] S. Kato, S.K. Matam, P. Kerger, L. Bernard, C. Battaglia, D. Vogel, M. Rohwerder, A. Züttel, Angew. Chem. Int. Ed. 55 (2016) 6028–6032.
[150] O. Sobol, F. Straub, Th. Wirth, G. Holzlechner, Th. Boellinghaus, W.E.S. Unger, Sci Rep 6 (2016) 19929.
[151] J. Zhang, Y. Zhang, M. Collin, S. Gin, J.J. Neeway, T. Wang, Z. Zhu, Surf Interface Anal 51 (2019) 219–225.
[152] B.E. Matthews, J.J. Neeway, L.N. Farias, J. Marcial, B.W. Arey, J. Soltis, L. Kovarik, Z. Zhu, M.J. Schweiger, N. Canfield, T. Varga, M.E. Bowden, J.L. Weaver, J.S. McCloy, R. Sjöblom, E. Hjärthner-Holdar, M. Englund, E. Ogenhall, E.P. Vicenzi, C.L. Corkhill, C. Thorpe, R.J. Hand, D.K. Peeler, C.I. Pearce, A.A. Kruger, Microscopy and Microanalysis 29 (2023) 50–68.
[153] T. Jia, Z. Zeng, H. Paudel, D.J. Senor, Y. Duan, Journal of Nuclear Materials 522 (2019) 1–10.
[154] X.-Y. Yu, J. Yao, B. Matthews, S.R. Spurgeon, S. Riechers, G. Sevigny, Z. Zhu, W. Jiang, W. Luscher, Journal of Materials Research and Technology 14 (2021) 475–483.
[155] R.G. Wilson, International Journal of Mass Spectrometry and Ion Processes 143 (1995) 43–49.
[156] M.C. Biesinger, D.J. Miller, R.R. Harbottle, F. Possmayer, N.S. McIntyre, N.O. Petersen, Applied Surface Science 252 (2006) 6957–6965.
[157] X. Vanden Eynde, K. Reihs, P. Bertrand, Macromolecules 32 (1999) 2925–2934.
[158] H. Min, S. Wettmarshausen, J.F. Friedrich, W.E.S. Unger, J. Anal. At. Spectrom. 26 (2011) 1157.
[159] I. Lanekoff, P. Sjövall, A.G. Ewing, Anal. Chem. 83 (2011) 5337–5343.
[160] T. Tanaka, K. Kawakami, S. Hayashi, J Mater Sci 49 (2014) 3928–3935.
[161] O. Sobol, G. Holzlechner, G. Nolze, T. Wirth, D. Eliezer, T. Boellinghaus, W.E.S. Unger, Materials Science and Engineering: A 676 (2016) 271–277.
[162] W.-C. Lin, H.-Y. Chang, K. Abbasi, J.-J. Shyue, C. Burda, Adv. Mater. Interfaces 4 (2017) 1600673.
[163] M.H. Philipsen, S. Sämfors, P. Malmberg, A.G. Ewing, Journal of Lipid Research 59 (2018) 2098–2107.
[164] X. Ren, L. Zou, X. Cao, M.H. Engelhard, W. Liu, S.D. Burton, H. Lee, C. Niu, B.E. Matthews, Z. Zhu, C. Wang, B.W. Arey, J. Xiao, J. Liu, J.-G. Zhang, W. Xu, Joule 3 (2019) 1662–1676.
[165] A. Röhsler, O. Sobol, H. Hänninen, T. Böllinghaus, Sci Rep 10 (2020) 3611.
[166] Z. Wang, K. Jin, Y. Zhang, F. Wang, Z. Zhu, Surf. Interface Anal. 46 (2014) 257–260.
[167] C.W. Magee, Journal of Vacuum Science & Technology A: Vacuum, Surfaces, and Films 1 (1983) 901–906.
[168] M.L. Yu, in: R. Behrisch, K. Wittmaack (Eds.), Sputtering by Particle Bombardment III, Springer Berlin Heidelberg, Berlin, Heidelberg, 1991, pp. 91–160.

[169] J. Zhang, J.J. Neeway, Y. Zhang, J.V. Ryan, W. Yuan, T. Wang, Z. Zhu, Nuclear Instruments and Methods in Physics Research Section B: Beam Interactions with Materials and Atoms 404 (2017) 45–51.
[170] Z. Zhu, V. Shutthanandan, Surf. Interface Anal. 44 (2012) 89–93.
[171] J. Sameshima, M. Yoshikawa, Surf Interface Anal 50 (2018) i–i.
[172] V.R. Deline, W. Katz, C.A. Evans, P. Williams, Applied Physics Letters 33 (1978) 832–835.
[173] K. Wittmaack, Journal of Applied Physics 52 (1981) 527–529.
[174] M.T. Bernius, S. Chandra, G.H. Morrison, Review of Scientific Instruments 56 (1985) 1347–1351.
[175] Y. Homma, Y. Ishii, Journal of Vacuum Science & Technology A: Vacuum, Surfaces, and Films 3 (1985) 356–360.
[176] A. Nishimoto, M. Koyama, S. Yamato, Y. Oda, T. Awane, H. Noguchi, ISIJ International 55 (2015) 335–337.